

1 Causes of Cretaceous subduction termination below South China and
2 Borneo: Was the Proto-South China Sea underlain by an oceanic plateau?

3

4 Suzanna H.A. van de Lagemaat^{1,*}, Licheng Cao², Junaidi Asis³, Eldert L. Advokaat¹, Paul R.D.
5 Mason¹, Mark J. Dekkers¹, Douwe J.J. van Hinsbergen¹

6

7 ¹Department of Earth Sciences, Utrecht University, Utrecht, the Netherlands

8 ²College of Marine Science and Technology, China University of Geosciences, Wuhan, China

9 ³Faculty of Science and Natural Resources, Universiti Malaysia Sabah, Kota Kinabalu, Malaysia

10

11 *Corresponding author: s.h.a.vandelagemaat@uu.nl

12

13 **Highlights**

- 14 - Comprehensive study of accreted ocean plate stratigraphy sequence in Sabah, Borneo
15 - Geochemical, geochronological, biostratigraphic, and paleomagnetic analyses
16 - Hypothesis that explains Mesozoic subduction cessation in the Proto-South China Sea
17 - Identification of a new 'Pontus' plate, below which the Izanagi Plate subducted

18

19 **Keywords:** Proto-South China Sea, Paleomagnetism, Geochemistry, Borneo, Paleo-Pacific,
20 Izanagi Plate

21

22 **This is a non-peer reviewed manuscript submitted to EarthArxiv. The manuscript has**
23 **been submitted for peer-review to *Geoscience Frontiers*. This is version 2 of this preprint.**

24 **Abstract**

25 The South China, Indochina, and Borneo margins surrounding the South China Sea contain long-
26 lived arcs that became inactive at approximately 85 Ma, even though an embayment of oceanic
27 crust (the 'Proto-South China Sea') remained in the intervening region. This oceanic crust
28 eventually subducted in the Cenozoic below Borneo and the Cagayan arc, while the modern
29 South China Sea opened in its wake. To investigate the enigmatic cessation of Mesozoic
30 subduction below South China and Borneo, we studied a fragment of oceanic crust and
31 overlying trench-fill sediments that accreted to NW Borneo during the final stages of Paleo-
32 Pacific subduction. Based on radiolarian biostratigraphy of cherts overlying the pillow basalts
33 and detrital zircon geochronology of the trench-fill, we constrained the minimum age of the
34 oceanic crust during accretion to 40 Ma. This shows that subduction cessation was not related
35 to ridge subduction. Geochemical analysis of pillow basalts revealed an enriched mid-ocean
36 ridge basalt signature comparable to oceanic plateaus. Using paleomagnetism, we show that this
37 fragment of oceanic crust was not part of the Izanagi Plate but was part of a plate (the 'Pontus'
38 Plate) separated from the Izanagi Plate by a subduction zone. Based on the minimum 40 Ma age
39 of the oceanic crust and its geochemistry, we suggest that Mesozoic subduction below South
40 China and Borneo stopped when an oceanic plateau entered the trench, while the eastern plate
41 margin with the Izanagi Plate remained active. We show how our findings offer opportunities to
42 restore plate configurations of the Panthalassa-Tethys junction region.

43

44 **1. Introduction**

45 For the last hundreds of millions of years, the East Asian margin has been accommodating
46 subduction of Paleo-Pacific (or 'Panthalassa') lithosphere (Isozaki et al., 1990; 2010). Today, the
47 subduction zone along the east Asian margin continues as far as Taiwan, where it connects to
48 plate boundaries of the Philippines. However, geological records of arc magmatism and
49 accretionary complexes show that until the Late Cretaceous (~80 Ma) a Paleo-Pacific
50 subduction zone was active along South China, through Hainan, Vietnam and Cambodia as far as
51 southern Borneo (e.g., Jahn et al., 1990; Lapierre et al., 1997; Xu et al., 1999; Shellnut et al., 2013,
52 2023; J. Li et al., 2014; Z. Li et al., 2014; Breiffeld et al., 2017, 2022; Hennig et al., 2017; Cao et al.,
53 2021; Nong et al., 2021, 2022; Hennig-Breiffeld et al., 2021; Waight et al., 2021; Hiu et al., 2022).
54 Then, around 80-70 Ma, Paleo-Pacific subduction at the SE China and Indochina margin appears
55 to have ceased, the South China and Vietnamese margins became passive, Paleogene rift basins
56 formed, and after the Eocene, the South China Sea extensional basin opened (Barckhausen et al.,
57 2014; C. Li et al., 2014; Morley, 2016; Wu et al., 2016; Ye et al., 2018). Why Cretaceous
58 subduction stopped, and where the ensuing convergence between the plates from the Pacific
59 realm and Eurasia was accommodated, is poorly known.

60 Clues as to why subduction ceased come from rock units of the subducted Paleo-Pacific
61 plates (Ocean Plate Stratigraphy (OPS); Isozaki et al., 1990) preserved in accretionary prisms.
62 Relics of Late Cretaceous and older prisms are found on Taiwan (Yui et al., 2012), along the
63 South China margin west of Taiwan (D. Zhou et al., 2006), and to the south of the South China
64 Sea in Palawan (e.g., Holloway, 1982; Shao et al., 2017; Fig. 1). The South China margin reveals
65 that during the final stages of subduction, lithosphere with seamounts as old as 154.1 ± 1.8 Ma
66 accreted (Xu et al., 2022). In addition, the Palawan record concerns a fragment of the South
67 China margin that became separated from its original position by opening of the South China
68 Sea basin within the SE China continental margin during the latest Eocene to middle Miocene
69 (Briais et al., 1993; Suggate et al., 2014; Li et al., 2015; Shao et al., 2017; Larsen et al., 2018). The
70 Eocene to Miocene opening of the South China Sea basin was accommodated by a southward-
71 dipping subduction zone below northern Borneo and the Cagayan arc (Hall, 2002; Hall and
72 Breitfeld, 2017) (Fig. 1C). Rock units that accreted during this southward subduction include
73 ~100 Ma old mafic rocks and Lower Cretaceous pelagic sediments (Dycoco et al., 2021; Muller,
74 1991) that are overlain by a continuous Upper Cretaceous (Campanian–Maastrichtian) pelagic
75 oceanic sequence and Eocene trench-fill sediments (Aurelio et al., 2014; Wolfart et al., 1986).
76 This shows that after Cretaceous subduction cessation at the South China-Borneo margin, there
77 oceanic lithosphere remained in the foreland embayment of the former subduction zone that
78 already existed before Cretaceous subduction cessation, and that remained in an oceanic
79 position until it was finally consumed by renewed subduction in the Eo-Oligocene. This oceanic
80 embayment that remained after Cretaceous subduction cessation and that was consumed
81 during Eocene to Miocene subduction below Borneo and the Cagayan arc is referred to as the
82 'Proto-South China Sea' (Tayler and Hayes, 1983; Hinz et al., 1994; Hall and Breitfeld, 2017).
83 Why the Proto-South China Sea remained in existence during the Late Cretaceous and early
84 Cenozoic while old oceanic lithosphere was still available to subduct (which eventually
85 subducted in the Eocene to Miocene) is puzzling.

86 Obtaining new geological data to decipher the enigmatic tectonic history of the Paleo-
87 Pacific/Proto-South China Sea from the deformed, poorly exposed, and largely submerged
88 records of the South China margin, Taiwan, and Palawan accretionary prisms is difficult due to
89 their poor preservation, accessibility, and tropical rainforest cover. However, the Proto-South
90 China Sea was also bordered by a former subduction zone associated with Paleo-Pacific
91 subduction to the south. Accretionary records related to this Paleo-Pacific subduction zone are
92 preserved in Sarawak (Serabang Complex, Lubok Antu Complex) and Sabah. There, an
93 accretionary complex expose OPS sequences consisting of pillow basalts, radiolarian cherts, and
94 trench-fill clastics (Jasin, 2000, 2018). These OPS sequences form the youngest part of a
95 Mesozoic accretionary prism adjacent to a Jurassic to Cretaceous volcanic arc exposed in

96 Kuching Zone (Breitfeld et al., 2017), and in the Schwaner Mountains (Hennig et al., 2017;
97 Breitfeld et al., 2020) of the SW Borneo Mega-Unit (Advokaat and Van Hinsbergen, 2023). This
98 prism and arc formed during northward motion of Borneo, as part of a plate carrying
99 continental fragments known as Argoland from the Gondwana margin towards Eurasia (Hall,
100 2012; Advokaat and Van Hinsbergen, 2023). Intriguingly, Borneo's northward motion towards
101 Eurasia stopped in the Late Cretaceous (Hall, 2012; Advokaat and Van Hinsbergen, 2023),
102 around the time of subduction cessation at the South China margin, 'trapping' oceanic crust in
103 the Proto-South China Sea embayment.

104 In this study, we investigate the age of the crust of the youngest OPS nappes exposed in the
105 Baliojong Complex in Sabah, North Borneo, using radiolarian biostratigraphy of the chert to
106 determine the minimum age of the oceanic crust, and detrital zircon geochronology of the
107 trench-fill deposits to constrain the age of its accretion. This allows us to determine the
108 minimum age of oceanic crust when it entered the subduction zone. We use major and trace
109 element geochemistry of pillow basalts to investigate the tectonic setting of formation of the
110 ocean floor. Finally, we use paleomagnetism of the pillow basalts and radiolarian chert to
111 constrain the paleolatitude of formation of the oceanic crust. This allows us to test possible
112 connections of the 'Proto-South China Sea' crust to the Tethyan or Paleo-Pacific paleo-plates. In
113 combination with available constraints from Palawan, the South China margin, and Taiwan, we
114 will evaluate possible reasons for the enigmatic cessation of long-lived subduction at the South
115 China-Sundaland margin, and the origin and destruction of the Proto-South China Sea.

116

117 **2. Geological setting**

118 **2.1. Records of arc magmatism related to Paleo-Pacific subduction**

119 A Mesozoic Paleo-Pacific subduction zone below SE China, Indochina and Borneo has been
120 interpreted based on evidence arc magmatism and accretionary complexes. Granitoid
121 emplacement in SE China occurred throughout the Mesozoic (e.g., X. Zhou et al., 2006; Ji et al.,
122 2017). For the suite of granites and related volcanics emplaced during the Late Jurassic and
123 Cretaceous it is generally accepted that they formed as a magmatic arc that formed during
124 subduction of Paleo-Pacific oceanic lithosphere (Jahn et al., 1976; Lapierre et al., 1997; Zhou and
125 Li, 2000; Li and Li, 2007; Zhou et al., 2006; H. Li et al., 2012; J. Li et al., 2014; Zhu et al., 2017;
126 Jiang et al., 2015; Liu et al., 2020; Sun et al., 2021). Most magmatism in SE China had ceased by c.
127 90 Ma, after which limited A-type magmatism occurred until 80 Ma, which was interpreted to
128 reflect extension (Li et al., 2012; Z. Li et al., 2014; J. Li et al., 2014; Liu et al., 2020). The youngest
129 granite intrusion, with a 73 Ma zircon U-Pb age is exposed on Hainan Island (Jiang and Li, 2014).

130 The youngest arc magmatism interpreted to be related to Paleo-Pacific subduction below
131 Indochina is most prominent in the Dalat Zone of Vietnam (e.g., Nguyen et al., 2004; Thuy et al.,

2004; Shellnut et al., 2013; Hennig-Breitfeld et al., 2021; Nong et al., 2022). Radiometric dating of these plutons using zircon and titanite U-Pb geochronology revealed ages from 122 to 75 Ma (Nguyen et al., 2004; Shellnutt et al., 2013; Hennig-Breitfeld et al., 2021; Nong et al., 2021). Based on the geochemistry of the igneous rocks in Vietnam and Cambodia, the older magmatic stage (110-89 Ma) that produced calc-alkaline I-type granitic batholiths, is thought to have formed during active subduction, while the younger magmatic stage (87-75 Ma) that produced A-type granites may instead relate to extensional deformation after subduction cessation (Shellnutt et al., 2013; Hennig-Breitfeld et al., 2021; Waight et al., 2021; Nong et al., 2022).

Westernmost Borneo (west Sarawak and NW Kalimantan) has been part of Sundaland since at least the Triassic (e.g., Breitfeld et al., 2017) and was possibly derived from South China (e.g., Metcalfe, 1985). Triassic and Jurassic magmatism and metamorphism in this part of Borneo was interpreted to be related to westward subduction of a Paleo-Pacific plate (Breitfeld et al., 2017; Hennig et al., 2017) predating accretion of the Proto-South China Sea. This sequence is unconformably overlain by Upper Jurassic shallow marine Bau limestone (Kakizaki et al., 2013), and by Upper Jurassic mudstone and radiolarian chert, and Cretaceous deep marine volcanoclastics of the Pedawan Formation (Breitfeld et al., 2017; Jasin and Said, 1999; Schmidtke et al., 1990; A. Zhang et al., 2022). This sequence was interpreted to record the transition from a passive margin in the Jurassic to a forearc basin in the Late Jurassic to Late Cretaceous (Breitfeld et al., 2017). The sequence is unconformably overlain by Upper Cretaceous (Maastrichtian) or Paleocene to Eocene continental clastics that post-date arc magmatism (Breitfeld et al., 2018; Berry, 2022).

SW Borneo, which was derived from Gondwana, preserves evidence of Jurassic magmatism that was interpreted as being related to rifting of the SW Borneo block (as part of 'Argoland') from Gondwana (Davies et al., 2014; Breitfeld et al., 2020; Batara and Xu, 2022). Subsequent magmatism related to Paleo-Pacific subduction below Gondwana-derived Borneo is well-exposed in the Schwaner Mountains of SW Borneo (e.g., Hennig et al., 2017; Breitfeld et al., 2017, 2020), and was underway by c. 132 Ma (Breitfeld et al., 2017, 2020), and perhaps already by 154-150 Ma (Batara and Xu, 2022). In North Borneo, arc magmatism was already active during the Triassic and Jurassic (Burton-Johnson et al., 2020), when the SW Borneo block was still part of the Gondwana margin (Hall, 2012; Advokaat and Van Hinsbergen, 2023). The youngest magmatism that may be related to Paleo-Pacific subduction exposed in the Schwaner Mountains has ages of c. 77 Ma (Breitfeld et al., 2017, 2020; Qian et al., 2022), but as in South China and Vietnam, A-type granite geochemical signatures in the post-80 Ma plutons in SW Borneo have also been interpreted as extensional magmatism that followed subduction cessation (Breitfeld et al., 2017, 2020).

167

168 **2.2. OPS records**

169 2.2.1. OPS records of Paleo-Pacific subduction

170 Information about the oceanic Paleo-Pacific lithosphere that was subducting below SE China
171 and Borneo comes from the accretionary prisms exposed in Taiwan, the northern South China
172 Sea margin, Palawan, and Borneo. There is no accretionary prism related to Paleo-Pacific
173 subduction exposed onshore in China or Vietnam.

174 Based on gravimetric, magnetic, and wide-angle seismic data, an accretionary complex was
175 interpreted in the NE margin of the South China Sea (Zhou et al., 2006). In this area, relics of two
176 seamounts have been found, which were originally interpreted as Miocene features (e.g., Wang
177 et al., 2012; Xu et al., 2020), but recently yielded plagioclase $^{40}\text{Ar}/^{39}\text{Ar}$ plateau ages of 154.1 ± 1.8
178 Ma and 93.2 ± 5.0 Ma (Xu et al., 2022). These seamounts have ocean island basalt (OIB)
179 geochemistry and are interpreted as intraplate basalts that formed on Paleo-Pacific lithosphere
180 (Xu et al., 2020, 2022). The oldest seamount thus provides a minimum age for the oceanic crust
181 (~ 154 Ma) of the Paleo-Pacific lithosphere that was subducting below SE China. The youngest
182 seamount provides a maximum age of accretion (~ 93 Ma), i.e., not long before the end of
183 subduction. Xu et al. (2022) suggested that these seamounts may have formed as part of an
184 oceanic plateau.

185 The submerged accretionary complex in the northern South China Sea may be contiguous
186 with the Tailuko Belt of Taiwan, which is interpreted as a Late Jurassic to Early Cretaceous
187 accretionary complex that formed during Paleo-Pacific subduction below the South China
188 margin (Yui et al., 2012). Here, upper Jurassic to lowermost Cretaceous terrigenous trench-fill
189 clastic sediments overlie Permian greenschist facies interlayers of marble, chert, and metabasite
190 (Yui et al., 2012), interpreted as an OPS sequence. The massive marbles are interpreted as
191 platform deposits, possibly deposited on seamounts or an oceanic plateau (Jahn et al., 1992; Yui
192 et al., 2012). The accretionary prism is intruded by Late Cretaceous granitic plutons, for which
193 ages of 90-87 Ma were obtained (Yui et al., 2009, 2012). The Tailuko Belt is unconformably
194 overlain by Eocene syn-rift sediments, which are interpreted as the passive margin sediments of
195 the northern South China Sea margin (Ho, 1986; Conand et al., 2020).

196 To the south of the South China Sea, the Palawan Continental Terrane is exposed on the
197 Palawan and Calamian Islands, in the Philippines. This 'continental' terrane is a composite
198 terrane that is also interpreted to have formed as an accretionary prism along the SE China
199 Margin (e.g., Holloway, 1982; Shao et al., 2017). After subduction ceased, the Palawan
200 Continental Terrane formed part of the SE China passive margin and was subsequently
201 transported southwards during opening of the South China Sea and became accreted in the
202 Cenozoic accretionary fold-thrust belt that formed north of the Cagayan arc during southward
203 subduction of the Proto-South China Sea (e.g., Cao et al., 2021). The Palawan Continental

204 Terrane exposed on the Calamian Islands comprises Permian to Upper Jurassic radiolarian
205 chert, middle Permian to Upper Jurassic limestone, and Middle Jurassic to Lower Cretaceous
206 trench-fill clastic sediments (Zamoras and Matsuoka, 2001, 2004). Based on the lithologic
207 transition from chert to limestone to terrigenous clastic sediments, it was interpreted that these
208 accreted units define a north-to-south younging accretionary prism, which formed during three
209 distinct accretion events in the Middle Jurassic, Late Jurassic, and Early Cretaceous (Zamoras
210 and Matsuoka, 2001, 2004). A Middle Jurassic to Late Jurassic accretionary prism is also
211 exposed on the island of Palawan (Faure and Ishida, 1990) and on the Buruanga Peninsula of
212 Panay (Zamoras et al., 2008). Detrital zircons in the trench-fill turbidites of the Palawan
213 Continental Terrane suggest a South China magmatic arc provenance (Cao et al., 2021). The
214 Palawan Continental Terrane is overlain by Upper Cretaceous continental clastic sediments
215 with arc-derived detrital zircons interpreted to have been deposited over the prism after
216 subduction ceased. The Upper Cretaceous continental clastics are overlain by Eocene syn-rift
217 turbidites with a South China provenance, which are interpreted to reflect the early opening
218 stages of the South China Sea basin. These are overlain by upper Oligocene-lower Miocene
219 limestones that formed during the drift of the Palawan Continental Terrane towards the
220 Palawan subduction zone. Finally, the early Miocene trench-fill clastic sediments date the arrival
221 of the Palawan Continental Terrane in the trench along the Cagayan arc (Steuer et al., 2013;
222 Aurelio et al., 2014; Suggate et al., 2014; Shao et al., 2017; Cao et al., 2021).

223 Sarawak exposes OPS-mélange with blocks of Upper Jurassic to Upper Cretaceous
224 radiolarian chert and Cretaceous trench-fill clastics (e.g., Jasin, 2000). U-Pb zircon detrital
225 zircon geochronology on the trench-fill sediments revealed maximum depositional ages
226 between 119 Ma and 88 Ma (Wang et al., 2021; Zhao et al., 2021). Similar mélange complexes
227 are also present in northern Sabah, where they comprise gabbro, plagiogranite, pillow basalt,
228 Cretaceous radiolarian chert, and trench-fill clastics (Jasin, 2000, 2018). Zircon U-Pb dating of
229 gabbro samples from these North Borneo accretionary complexes, of which the (tectono-
230)stratigraphic context is not well known, yielded mean ages between 112 ± 2 and 123 ± 1 Ma and
231 basalt samples yielded $^{40}\text{Ar}/^{39}\text{Ar}$ plateau ages of $\sim 134.5\pm 2.8$ and 135.9 ± 2.2 Ma (Wang et al.,
232 2023). Trench-fill sandstones yielded maximum depositional ages of ~ 114 Ma, based on detrital
233 zircon geochronology (Wang et al., 2023). The OPS mélanges in North Borneo are
234 unconformably overlain by middle Eocene sandstones (Hutchison, 1996; Hutchison et al., 2000;
235 Jasin and Tongkul, 2013; Van Hattum et al., 2013; Rahim et al., 2017) that farther to the north
236 were incorporated into a north-vergent fold-thrust belt known as the Rajang-Crocker
237 accretionary prism that formed during southward subduction below north Borneo along-strike
238 of Palawan (Van Hattum et al., 2006, 2013; Lambiase et al., 2008).

239

240 2.2.2. OPS records of the Proto-South China Sea

241 Information about the Proto-South China Sea, which is the oceanic lithosphere that was
242 preserved after Mesozoic subduction cessation, comes from the OPS sequence exposed in
243 Palawan. These sequences are found thrust over the Palawan Continental terrane, and, in
244 turn, are overthrust by supra-subduction zone ophiolites with latest Eocene metamorphic
245 soles showing that they accreted in a late Eocene and younger subduction zone before the
246 arrival of the Palawan Continental Terrane in the trench (Schlüter et al., 1996; Aurelio et al.,
247 2014; Dycoco et al., 2021). These ophiolites were interpreted to have formed by inversion of a
248 mid-oceanic ridge (Keenan et al., 2016), but regional kinematic restoration makes it more likely
249 that they formed in the forearc of a subduction zone along the northern SW Borneo continental
250 block, which includes the basement of the Cagayan arc (Advokaat and Van Hinsbergen, 2023).
251 The thrust vergence of the accreted rock units of Palawan is northward, showing geological
252 evidence for southward Proto-South China Sea subduction (Hall, 2002; Keenan et al., 2016).
253 Based on seismic tomographic interpretations, Wu and Suppe (2018) suggested that also an Eo-
254 Oligocene northward subduction zone may have existed within the PCSC, but there is no
255 evidence for this interpretation in the geological record.

256 The OPS sequences that are tectonically sandwiched between the Palawan Continental
257 Terrane and the Palawan Ophiolite, are somewhat confusingly known as the 'Southern Palawan
258 Ophiolite' (Gibaga et al., 2020; Dycoco et al., 2021), but are not associated with metamorphic
259 sole rocks and are instead interpreted as off-scraped relics of a subducted, oceanic lithosphere.
260 The Southern Palawan Ophiolite was assigned a Mesozoic age based on the presence of Early
261 Cretaceous nannoplankton in calcareous red clay associated with pillow basalts (Muller, 1991)
262 and Upper Cretaceous radiolarian cherts (Wolfart et al., 1986). In addition, float samples of
263 gabbro and syenite, interpreted to have been derived from the Southern Palawan Ophiolite,
264 yielded 100.7 ± 1.2 Ma and 103.0 ± 1.1 Ma zircon U-Pb ages (Dycoco et al., 2021). Whether these
265 samples are derived from the gabbroic section of the South Palawan Ophiolite or from
266 intrusions into it is unknown, but the obtained ages provide minimum ages of the oceanic
267 lithosphere of the Proto-South China Sea (Dycoco et al., 2021), which thus must already have
268 existed prior to the cessation of subduction at the south China Sea margin. This falsifies
269 hypotheses that propose that the Proto-South China Sea represents a Paleocene back-arc basin
270 (e.g., Zahirovic et al., 2014). The volcanic section and the gabbroic float samples of the South
271 Palawan Ophiolite have an ocean island basalt geochemical affinity, while a mafic dike has an
272 island arc signature (Gibaga et al., 2020; Dycoco et al., 2021). Peridotites of the South Palawan
273 Ophiolite have signatures transitional between Mid-Ocean Ridge Basalt (MORB) and Island Arc
274 Tholeiite (IAT) and are interpreted to have formed in a supra-subduction zone environment
275 (Labis et al., 2021).

276 The Proto-South China Sea was also lost to oblique eastward subduction below northern
277 Luzon (e.g., Hall, 2002) and fragments of its oceanic crust may be preserved in the Philippines
278 (Yumul et al., 2020). In western Luzon, a highly sheared mélange with a serpentinite matrix and
279 blocks of Lower Cretaceous radiolarian cherts is exposed to the west of the Zambalas Ophiolite,
280 referred to as the West Luzon Shear Zone (Karig, 1983). A similar serpentinite-matrix mélange
281 (the Dos Hermanos Mélange), with uppermost Jurassic to Lower Cretaceous radiolarian chert is
282 exposed in the northwest of Luzon, in the Ilocos Norte region (Queaño et al., 2017). Geochemical
283 signatures of the Dos Hermanos Mélange ultramafic and mafic rocks display MORB and island
284 arc signatures and are interpreted to have formed in a supra-subduction setting (Pasco et al.,
285 2019).

286

287 **3. Methods, results, and interpretation**

288 We collected samples from an OPS sequence in the Cretaceous accretionary prism of Sabah,
289 north Borneo. This OPS section forms part of a series of rocks in NW Borneo that is sometimes
290 referred to as the Chert-Spilitite formation, a somewhat outdated term (see Jasin, 1991,
291 Hutchison, 2005). We performed fieldwork at a well-exposed section along the Baliojong River,
292 northeast of Kota Marudu (Fig. 2 and 3). The rocks in this section are the youngest known
293 accreted OPS units prior to the Eocene and younger Rajang-Crocker accretionary prism, and are
294 hence presumably youngest parts of the Mesozoic accretionary prism exposed in Borneo. We
295 studied five sequences of OPS (B2-B5) that are exposed in thrust fault-bounded, coherent
296 stratigraphic sections comprising pillow basalts with overlying radiolarian chert and trench-fill
297 turbidites consisting of fine- to coarse-grained sandstone (Jasin and Tongkul, 2013). In a few
298 instances, the oldest part of the deep marine sediments consists of a rhythmic alternation
299 between radiolarian chert and red siltstone. We documented five sections from fault-bounded
300 thrust slices. Each section is overturned with dips typically between 25 and 50° (115-140°), but
301 with local variation due to folding. In sections 2 and 3, the trench-fill clastic sediments were
302 truncated from the OPS sequence along footwall cutoffs. Based on field relationships, it was not
303 possible to conclusively demonstrate whether all thrust slices represent a duplexed series of a
304 single accreted OPS sequence, or whether there are multiple OPS sections that accreted at
305 different times. From four sections (B2-B5) we collected samples for geochemical analyses from
306 pillow lavas, for radiolarian stratigraphy from chert sections, for paleomagnetic analyses from
307 both pillow lavas and red clays intercalated in the basal chert sections, and finally, from two
308 sections (B2 and B5) we collected turbiditic sandstones for sediment provenance and maximum
309 depositional age analysis. Below, we describe the results and first-order interpretation per data
310 type.

311

312 **3.1. Basalts: major and trace element geochemistry**

313 **3.1.1. Sampling and methods**

314 We collected 22 samples of basaltic pillow lavas from sections 2, 3, 4, and 5 (See Fig. 2 for
315 locations). Samples were crushed using a steel jaw crusher and ground in a tungsten carbide
316 mill. Loss on ignition (LOI) was measured at 1000°C by thermo-gravimetric analysis. Fusion
317 beads were prepared for whole rock x-ray fluorescence (XRF) major element analysis using 0.6
318 g sample and 6 g of flux consisting of 66% lithium tetraborate, 34% lithium metaborate and
319 0.5% lithium iodide. Wavelength dispersive XRF measurements for major elements were done
320 sequentially with a Thermo Scientific ARL Perform'X 4200W instrument at Utrecht University,
321 the Netherlands. Results were reported on a loss-free basis.

322 Trace elements were measured by laser ablation inductively coupled plasma-mass
323 spectrometry (LA-ICP-MS) on the fusion beads using a GeoLas 200Q 193nm ArF Excimer laser
324 ablation system coupled to a Thermo Finnigan Element2 sector field ICP-MS at Utrecht
325 University. Fusion beads were ablated with a fluence of 12 Jcm⁻², a pulse repetition rate of 10Hz
326 and with a crater diameter of 120 µm. Calibration was performed against NIST SRM 612 glass
327 using standard data reduction protocols (Longerich et al., 1996) and accuracy was monitored
328 using the USGS basaltic glass standard BCR2-G.

329 Three basaltic standard reference materials, BIR-1, JB-1B and JB-2 were treated as
330 external standards and were measured in parallel with the basaltic rocks collected in this study.
331 Results are reported alongside the samples in Table 1 and show excellent agreement with
332 recommended values from the GEOREM database (Jochum et al., 2005), to within 10% of
333 recommended values for most elements measured.

334

335 **3.1.2. Results and Interpretation**

336 Eighteen samples plot as basalts on the total alkali-silica diagram (Le Bas et al., 1986) and four
337 have slightly elevated SiO₂, plotting in the basaltic andesite field. Major elements such as MgO,
338 Al₂O₃ and CaO vary across this range in SiO₂ consistent with minor degrees of fractional
339 crystallization (Table 1). Loss on ignition was typically below 5%, but some samples showed
340 elevated LOI and/or an increase Na₂O and K₂O that reflects minor post-magmatic alteration
341 (Table 1). Increased concentrations of alkalis compromise the use of these elements in tectonic
342 discrimination diagrams. In contrast, immobile trace element ratios and relative abundances
343 are consistent with a mid-ocean ridge basalt (MORB) origin, for example using Zr vs Ti, Ti/Y vs
344 Zr/Y and Ti/1000 vs V (Fig. S1; Rollinson et al., 2021). Rare earth element abundances further
345 constrain the tectonic setting and are consistent with a slightly enriched E-MORB origin, with
346 Ce/Yb_N equal to or > 1 (Fig. S2).

347 Samples from the four thrust sheets show distinctive trace element compositions with
348 variable degrees of enrichment seen between the sampled locations, reflecting variable degrees
349 of input from N-MORB and E-MORB mantle sources. This is shown most clearly on a plot of
350 Th/Yb vs Nb/Yb where variable enrichment is seen around average E-MORB (Fig. 4; Pearce,
351 2008). There is no evidence for fluid-modified melting or melting of more enriched OIB mantle
352 sources in the source of the basalts that we sampled. In summary, the basalts were produced by
353 melting of an enriched MORB source, coupled with minor degrees of fractional crystallization.
354 These data would be consistent with an origin in an oceanic plateau, although a mid-oceanic
355 ridge setting is not excluded.

356

357 **3.2. Radiolarian cherts: biostratigraphy**

358 **3.2.1. Sampling and methods**

359 We collected 29 samples of radiolarian chert and red cherty siltstone from the Baliojong
360 River OPS, nine samples from section BC2, ten samples from section BC3, and ten samples from
361 section BC5, to complement earlier biostratigraphic results for the Baliojong River section of
362 Jasin and Tongkul (2013). All samples were crushed into small fragments (1cm to 2cm), which
363 were subsequently dissolved using dilute hydrofluoric acid 5% and water, with a ratio of acid to
364 water of 1:9 and soaked for about 24 hours (the concentration of acid and the time of treatment
365 varied slightly, depending on the sample) (Pessagno and Newport, 1972). After that all samples
366 were rinsed with fresh water and dried before they were examined under the microscope. Well-
367 preserved specimens were photographed using scanning electron microscopy (SEM) for further
368 examination.

369

370 **3.2.2. Results and interpretation**

371 The classification, taxonomy and biostratigraphic range of the radiolarian species are based
372 on Sanfilippo and Riedel (1985), Thurow (1988), Vishnevskaya (1993) and O'Dogherty (1994).
373 All samples collected contain radiolarian skeletons that are moderately to well-preserved. The
374 amount of radiolarian skeletons in the red siltstone samples was much lower than in the
375 radiolarian chert samples. We identified a total of 62 radiolarian species and some selected
376 radiolarian species are portrayed in Fig. S3.

377 The biostratigraphic analysis of the radiolarian species, which is described in detail in
378 Supporting Information 1, reveals two assemblages of radiolarian species that are identified in
379 all three sections (Fig. 5). Assemblage I ranges in age from Barremian to Aptian (Early
380 Cretaceous (i.e., 126.5-113.2 Ma) and is represented by samples BC2.9 to BC2.5 in Section BC2,
381 samples BC3.10 to BC3.4 in section B3 and samples BC5.10 to BC5.3 in Section BC5. Assemblage
382 II is indicative of Albian to Cenomanian age (Early to Late Cretaceous, i.e. 113.2-93.9 Ma) and is

383 recorded in samples BC2.4 to BC2.1 in section BC2, samples BC3.3 to BC3.1 in section B3 and
384 sample BC5.2 and BC5.1 in section BC5. This confirms previous biostratigraphic results of Jasin
385 and Tongkul (2013) and shows that the E-MORB basalts of the Baliojong River section formed in
386 Early Cretaceous times, and must have formed on an ocean floor that predated this age.

387

388 **3.3. Foreland basin clastics: Detrital zircon geochronology and provenance**

389 **3.3.1. Sampling and methods**

390 We collected a total of twelve samples from turbiditic sandstones: seven samples (BF2.1 to
391 BF2.7) from section B2 of and five samples (BF5.1 to BF5.5) from section B5; sections B3 and B4
392 do not contain sandstone. As shown in representative thin section photomicrographs (Fig. S4),
393 samples of section BF2 are quartzose sandstones composed of angular to sub-angular quartz
394 with feldspar, sericite, and chert clast, whereas those of section BF5 are calcite-bearing lithic
395 arenites. These samples were prepared for whole-rock geochemical analysis, heavy mineral
396 analysis and detrital zircon single-grain geochronology using procedures described in
397 Supporting Information 2.

398

399 **3.3.2. Results**

400 **3.3.2.1. Whole-rock geochemistry**

401 The results of major and trace element analyses of the sandstone samples are provided in
402 Table 2. In the ternary diagram of relative proportions of Ca, Al, and Si (Fig. 6A), samples of
403 section BF2 plot near the Si apex, showing dominance of detrital silicates therein. In contrast,
404 samples of section BF5 are separate from this cluster due to a varying degree of Ca dilution
405 (31.8%–0.8%), which correlates with authigenic components therein. This compositional
406 difference is also observed in the Upper Continental Crust (UCC; Rudnick and Gao, 2003)-
407 normalized elemental distributions (Fig. 6B). Samples of section BF2 display slight enrichment
408 of Mn, Zr, and Hf and strong depletion of Ca and Na, whereas strong enrichment of Ca and Mn
409 and slight depletion of Zr and Hf in samples of section BF5 confirm the dilution by authigenic
410 components. In addition, samples of the two sections show a varying degree of depletion of
411 large-ion lithophile elements (e.g., K, Rb, Sr, Cs, and Ba) and high field-strength elements (e.g.,
412 Nb, Th, and U). In the distribution of chondrite-normalized (Sun and McDonough, 1989) rare
413 earth elements (REE), samples of the two sections are comparable in showing moderate light-
414 REE enrichment and negative Eu anomalies, with average $\sum\text{LREE}/\sum\text{HREE}$ and δEu
415 $((\text{Eu}/\sqrt{\text{Sm} * \text{Gd}})_N)$ values of 6.1 and 0.7, respectively (Fig. 6C). The REE concentrations of
416 section BF5 (average 131.3 ppm), because of relatively enriched middle and heavy-REEs, are
417 systematically higher than those of section BF2 (average 88.7 ppm), which could be caused by
418 the preferential adsorption of REEs in more fined-grained sediments of section BF5. Among all

419 samples, sample BF5.1 features the largest REE concentration (240.2 ppm) and strong light-REE
420 enrichment relative to heavy-REE with a $(La/Lu)_N$ ratio of 11.1.

421 Geochemical data are also plotted in different diagrams for compositional discrimination (Fig.
422 6D-G). The Hf-La/Th and Zr/Sc-Th/Sc plots show increasing old components and corresponding
423 sediment recycling for samples of section BF2 (Fig.6D-6E), which is consistent with their slight
424 Hf and Zr enrichment observed in the UCC-normalized curves (Fig. 6B). In contrast, most
425 samples of section BF5 have a geochemical affinity of an andesitic arc source with limited
426 influence of sediment recycling. Samples between sections BF2 and BF5 are further
427 discriminated by ferromagnesian elements with the former and the latter plotting towards
428 more mafic and felsic source endmembers, respectively (Fig. 6F-G). Likewise, Cr and Ni in
429 samples of section BF2, compared to UCC, are highly enriched by a factor of up to 17.5 and 14.3,
430 respectively (Fig. 6B). The major element-based discriminant function diagram (Roser and
431 Korsch, 1988) does not perform well in provenance discrimination and samples show a
432 scattered distribution between the fields of mafic and intermediate sources (Fig. 6F)

433

434 **3.3.2.2. Heavy minerals**

435 Samples of sections BF2 and BF5 show great difference in heavy mineral compositions (Fig.
436 7, Table 3). The mineral assemblages in section BF2 are consistent, with dominant zircon
437 (average 50.6%) and pyrite (average 23.3%) as well as a minor percentage of rutile, Cr-spinel,
438 and leucoxene. Sample BF2.7 also contains abundant hematite-limonite. In contrast, the mineral
439 compositions significantly vary in section BF5. While the mineral assemblage of sample BF5.2 is
440 comparable to that of section BF2, sample BF5.1 and samples BF5.4 and BF5.5 are dominated by
441 ilmenite (87.8%) and pyrite (average 80.1%), respectively. Compared to the moderate to high
442 percentage of stable minerals (including zircon, tourmaline, and rutile) in section BF2, the
443 commonly lower values in section BF5 suggest lower compositional maturity due to the lack of
444 detrital components therein.

445

446 **3.3.2.3. Detrital zircon geochronology**

447 A total of 640 zircon grains from sections BF2 and BF5 were analyzed in this study. The
448 results of zircon single-grain analyses of sandstone samples, including U-Pb geochronology,
449 geochemistry, grain size and shape, are provided in Table S2. Detrital zircon age signals within
450 each section show a varying degree of inter-sample variation (Fig. 8). In section BF2, samples
451 BF2.3 and BF2.5 consistently show strong age peaks at ca. 115 Ma and 240–235 Ma, a
452 subordinate peak at ca. 450–430 Ma, as well as a scattered distribution of Proterozoic ages. The
453 age signals of samples BF2.1 and BF2.7 are slightly different from the above pattern, with a
454 larger percentage of Cretaceous ages and fewer Proterozoic ages in the former and an implicit

455 peak of Ordovician-Silurian (i.e., mid-Paleozoic) ages in the latter. Greater inter-sample variety
456 of age signals is observed in section BF5. Samples BF5.2 and BF5.5 feature a near unimodal
457 signal with dominance of Jurassic-Cretaceous ages and a scattered distribution of more ancient
458 ages. The Jurassic cluster peaking at ca. 150 Ma is also seen in sample BF5.4, albeit with
459 subordinate peaks at ca. 225 Ma, 435 Ma, and 1840 Ma. In contrast, sample BF5.1 features an
460 Early Cretaceous cluster peaking at ca. 120 Ma and a weak Caledonian peak. Samples within
461 each section are grouped to characterize their overall age signals. Along with the common
462 occurrence of the Caledonian cluster and scattered Proterozoic ages, sections BF2 and BF5 are
463 clearly discriminated by a moderate lull and a strong peak of Jurassic ages, respectively.

464

465 **3.3.3. Interpretation**

466 The radiolarian biostratigraphic ages of the Baliojong OPS reveal that the foreland basin
467 clastics are younger than Albian-Cenomanian (Jasin and Tongkul, 2013; see section 3.2). We use
468 the U-Pb detrital zircon ages to establish the maximum depositional age of the foreland basin
469 clastics (Dickinson and Gehrels, 2009), which in accretionary orogens adjacent to active arcs are
470 typically close to the depositional age (Cawood et al., 2012).

471 We calculate maximum depositional ages using eight proxies: (i) the youngest single grain
472 age (YSG); (ii) the 'youngest detrital zircon' age calculated by Isoplot (YDG; Ludwig, 2003); (iii)
473 the maximum likelihood age calculated by IsoplotR (MLA; Vermeesch, 2021); (iv) the weighted
474 mean age of three youngest grains (YG(3); Zhang et al., 2015); (v) the weighted mean age of the
475 youngest cluster with two or more grains overlapping in age at 1σ (YGC $1\sigma(2+)$; Dickinson and
476 Gehrels, 2009); (vi) the weighted mean age of the youngest cluster with three or more grains
477 overlapping in age at 2σ (YGC $2\sigma(3+)$; Dickinson and Gehrels, 2009); (vii) the weighted mean
478 age of the youngest cluster with a mean square weighted deviation (MSWD) of ~ 1 (YSP; Coutts
479 et al., 2019); (viii) the youngest graphic peak age of the kernel density estimation (KDE)
480 spectrum (YPP).

481 Among 640 zircon grains analyzed in this study, two concordant grains (BF2.5-45 and
482 BF5.5-45) are dated with Eocene ages (36.6 Ma and 41.6 Ma) with one containing a very high U
483 concentration of 3056.3 ppm (Table S2). The rare existence of these abnormally young ages
484 contrasts with the ages of the unconformably overlying Crocker Formation and cannot
485 represent the sedimentary age of the foreland basin clastics (Hall and Breiffeld, 2017; Jasin and
486 Tongkul, 2013). Moreover, [the Crocker formation has a distinctly different geochronological signal
487 in the absence of Neoproterozoic and Ordovician-Silurian zircons](#) (Fig. S5). We infer that these
488 Eocene grains may potentially be influenced by Pb loss, and we excluded them in the calculation
489 of maximum depositional ages.

490 Different proxies of maximum depositional ages of sandstone samples range from 109.0 Ma
491 to 79.9 Ma in section BF2 and from 114.0 Ma to 86.3 Ma in section BF5, but they do not
492 explicitly show a younging or aging trend within each section (Fig. 9). Age proxies roughly
493 cluster in samples BF2.1, BF5.2, and BF5.5 and the age estimates through the YSG, YDG, and
494 MLA approaches are younger than the other proxies.

495 Following the data treatment strategy of Rinke-Hardekopf et al. (2021), regardless of the
496 choice of age proxies, the calculated maximum depositional ages mostly belong to the Late
497 Cretaceous and individual age proxies of section BF2 are about 6 Ma younger than those of
498 section BF5. The interpretation of different depositional ages between the two sections is
499 consistent with their different signatures of whole-rock geochemistry, heavy minerals, and
500 zircon U-Pb ages (Figs. 6, 7, 8). Considering the potential Pb loss effect for youngest single
501 grains and the conservative nature of age proxies based on multiple grains, we select the
502 YGC2 σ (3+) proxy to represent the maximum depositional age, which is 86.8 Ma in section BF2
503 and 92.9 Ma in section BF5 (Fig. 9). Thus, the Baliojong turbidites were likely deposited around
504 the Turonian–Coniacian, which is reasonably younger than the underlying Albian–Cenomanian
505 cherts and Early Cretaceous basalts (Jasin and Tongkul, 2013; Wang et al., 2023).

506

507 **3.4. Paleomagnetism of basalts and pelagic sediments**

508 **3.4.1. Sampling and methods**

509 We collected core samples with a standard diameter of 25 mm for paleomagnetism using a
510 petrol-powered drill from pillow basalts and cherts. A total of 147 pillow basalt samples (coded
511 PB) was collected from sections B2, B3, and B4, and 48 samples were collected from red
512 siltstones (coded PC) intercalated in the basal parts of the chert sequence in sections B2, B3, and
513 B5 (Fig. 2 and 3C). The pillow basalt section of section B5 was of insufficient stratigraphic
514 thickness to collect enough samples that would accurately sample paleosecular variation, while
515 section B4 did not contain the rhythmic alternation of red siltstone and radiolarian chert. The
516 orientation of the samples was measured in the field with a magnetic compass and inclinometer
517 attached. Following sampling procedures for paleomagnetic poles recommended in Gerritsen et
518 al. (2022), we collected a single core per basalt pillow or siltstone bed to optimize the chance of
519 sampling individual spot readings of the paleomagnetic field with each core. The pillow basalt
520 sections were generally sufficiently thick to collect about 50 samples over at least 100m of
521 stratigraphy. Ten to twenty red siltstone samples were collected per section, from exposures of
522 a few meters in thickness. Estimated bedding attitudes of pillow basalts are generally striking
523 roughly N-S with a $\sim 45^\circ$ overturned dip. Our bedding estimates of the pillow basalts were like
524 those measured in the directly overlying radiolarian cherts, although our estimation was
525 somewhat steeper. As the bedding attitude of pillow basalts is difficult to measure, and as

526 pillows may have a small primary dip, we will discuss how the use of the bedding attitudes of
527 the radiolarian chert alters our results.

528 Paleomagnetic analyses were carried out at the paleomagnetic laboratory Fort Hoofddijk at
529 Utrecht University, the Netherlands. The pillow basalt samples were subjected to stepwise
530 alternating field (AF) demagnetization in a robotized setup (Mullender et al., 2016) and the red
531 siltstone samples were subjected to stepwise thermal (TH) demagnetization. The magnetization
532 of all samples was measured on a 2G DC-SQUID magnetometer. During this process, the samples
533 were kept in a magnetically shielded room.

534 We used the online portal Paleomagnetism.org (Koymans et al., 2016, 2020) for sample
535 interpretation and statistical analysis. Demagnetization diagrams were plotted as orthogonal
536 vector diagrams (Zijderveld, 1967) and magnetic components were determined using principal
537 component analysis (Kirschvink, 1980). Components decaying towards the origin are not forced
538 to the origin, except when demagnetization diagrams are noisy. We did not apply a maximum
539 angular deviation cutoff, as it does not demonstrably influence the precision or position of a
540 pole (Gerritsen et al., 2022), but the widely used cutoff of 15° would not have eliminated data.
541 Site mean directions were calculated using Fisher (1953) statistics on virtual geomagnetic poles
542 following statistical procedures described in Deenen et al. (2011). To support the
543 paleomagnetic results, thermomagnetic analysis was carried out with a modified horizontal
544 translation Curie balance (Mullender et al., 1993) on selected samples to shed light on the
545 dominant magnetic minerals. In the thermomagnetic analysis samples were stepwise heated to
546 700 °C in air with intermittent cooling segments to distinguish thermochemical alteration from
547 magnetic behavior. The Curie temperature is estimated with the two-tangent method (Grommé
548 et al., 1969). The temperature sequence is as follows for the pillow basalts (in a cycling field
549 between 200 and 300 mT): room temperature – 150 °C – 70 °C – 250 °C – 150 °C – 350 °C – 250
550 °C – 450 °C – 350 °C – 520 °C – 420 °C – 620 °C – 500 °C – 700 °C – room temperature. For the
551 red silts it is (in a cycling field between 50 and 300 mT): room temperature – 250 °C – 150 °C –
552 350 °C – 250 °C – 450 °C – 350 °C – 520 °C – 420 °C – 620 °C – 500 °C – 700 °C – room
553 temperature. To check for hematite behavior in a non-saturated applied field a second sample
554 was stirred in the Curie balance sample holder after the 250 °C – room temperature partial run
555 after which the complete stepwise thermomagnetic run was done (cf. De Boer and Dekkers,
556 1998).

557

558 **3.4.2. Results and interpretation**

559 In the thermomagnetic analysis, pillow basalts showed a gradual magnetization decay with
560 minor removal of magnetic moment during the experiment, typical of maghemite that partly
561 converts to less magnetic hematite (Fig. 10A). The Curie temperature is estimated at ~610 °C.

562 Sample PB2.11 has this behavior to a greater extent than sample PB3.18 which reveals
563 reversible magnetic behavior. This indicates that the maghemite (presumably thermally
564 stabilized by some substituted Ti or Al) is probably formed in nature (i.e., not during the
565 experiment itself). During the final cooling from 700 °C most maghemite converts to hematite as
566 testified by the much lower final magnetization.

567 As expected, the red silts are much weaker (~10 to ~100 times) than the pillow basalts. The
568 thermomagnetic behavior is dominated by hematite as indicated by the Néel temperature at
569 675 °C (Fig. 10B). Because high-coercivity hematite is not magnetically saturated in a field of
570 300 mT, the cooling segments are above the corresponding heating segments (Fig. 10B). This is
571 an expression of acquisition of a magnetic moment and not of thermochemical alteration, as
572 demonstrated by the stirring experiment in sample PC3.3. After the partial run to 250 °C,
573 stirring of the sample when back at room temperature, the second run (again to 250 °C and then
574 according to the full thermomagnetic experiment procedure) starts at approximately the same
575 magnetic moment as at the beginning of the first run and not at the final magnetic moment of
576 the first run. This indicates that the increase has a magnetic cause and is not induced by
577 thermochemical alteration (De Boer and Dekkers, 1998). Rather surprisingly, magnetite – the
578 carrier of the NRM signal – is below the limit of detection albeit that magnetite is formed during
579 heating between 600 and 700 °C as manifested by marked increase in magnetic moment during
580 cooling below 550 °C on the final cooling run. Sample PC3.3 shows this behavior to a larger
581 extent than sample PC2.10 (Fig. 10B).

582 The NRM of the red silt samples shows a large secondary component up to ~200 °C (Fig.
583 10B). We speculate that this may be associated with the relatively large increase during the
584 cooling segments in the thermomagnetic experiments after 250 and 350 °C, while the increase
585 after cooling at higher temperatures up to 520 °C is barely noticeable (Fig. 10B). It would
586 indicate a big proportion of very fine-grained hematite with low unblocking temperatures.

587 Samples from pillow basalts had initial NRM intensities ranging from 0.2 to 1.0 A/m,
588 whereas the red silts had much lower intensities ranging from 200 to 2000 $\mu\text{A}/\text{m}$. Alternating
589 field (AF) demagnetization in the pillow basalt (PB) samples generally shows a low coercivity
590 component, followed by linear demagnetization trends towards the origin on the Zijderveld
591 diagram (Fig 11A). Maximum unblocking fields for the basalts mostly occur around 100 mT. In
592 addition, at fields of 40-50 mT, a small component appears that deviates the trend away from
593 the origin, which is interpreted as a laboratory-induced gyroremanent magnetization (GRM)
594 (Dankers and Zijderveld, 1981). The datapoints influenced by GRM were not used to interpret
595 the Characteristic Remanent Magnetization (ChRM). ChRM directions were interpreted based
596 on a minimum of four consecutive data points.

597 The Zijderveld diagrams of the cherty siltstone samples (PC) are noisier than those of the
598 basalts, but it is in most cases possible to discern a low-temperature component that is distinct
599 from a high-temperature component that decays towards the origin (Fig 12A). In the case of the
600 pillow basalts, the high-coercivity component has northeasterly declinations (Fig 11B), while in
601 the case of the cherty siltstones, the high-temperature component has southerly declinations
602 (Fig 12B). We interpret these high-coercivity (PB sample set) or high-temperature (PC sample
603 set) components as the ChRM directions. The ChRM directions of the pillow basalts were
604 generally interpreted in the range of 30-50 mT. In some cases, the ChRM direction was already
605 isolated from as low as 15 mT up to as high as 120 mT. ChRM directions of red siltstones were
606 interpreted mostly in the range 250-510°C, but could sometimes be interpreted up to 580°C. It
607 was possible to isolate a ChRM from most PB and PC samples, although a few samples were
608 rejected due to erratic demagnetization behavior or strongly deviant paleomagnetic directions
609 that we interpreted as the result of orientation errors or lightning strikes when a sample was
610 almost completely demagnetized below 20 mT. Including these directions in the grand average
611 would not have significantly shifted the computed paleomagnetic poles.

612 Mean paleomagnetic ChRM directions for all sites in geographic and tectonic (corrected for
613 bedding tilt) coordinates are listed Table 4 and shown in Fig. 11B and 12B. All interpreted
614 pillow basalt (PB) samples indicate the same polarity and the mean ChRM directions of the PB
615 sites are different from the present-day GAD field in both geographic and tectonic coordinates
616 (Fig. 11B). There is a slight variation in mean paleomagnetic direction between PB sites. In
617 geographic coordinates, the directions of all three sections are significantly different (no
618 Common True Mean Direction; CTMD; Tauxe et al., 2010) and vary by $\sim 15^\circ$ in declination and
619 inclination. In tectonic coordinates, the different PB sites also do not share a CTMD, but the
620 variation in declination is smaller, up to maximum 8° (Table 4), while the inclination of PB2 is
621 significantly steeper than for PB3 and PB4 ($I = -26.9 \pm 6.9^\circ$ in PB2 versus $I = -4.9 \pm 7.2^\circ$ in PB3 and
622 $8.9 \pm 7.1^\circ$ for PB4). Fold tests per section are inconclusive (Tauxe and Watson, 1994;
623 implemented in Paleomagnetism.org). When PB2 and PB3 are combined, the fold test is
624 negative, but PB2 and PB4, as well as PB3 and PB4 yield an optimal clustering at $\sim 90\%$
625 unfolding (Fig. 11C). When all sites are combined, the fold test is inconclusive (Fig. 11C).

626 The red siltstone (PC) samples have an opposite polarity to the basalts (Fig. 12B). In
627 geographic coordinates, the three sampled sections yield similar direction clusters, with
628 average declinations varying from $D = 163.8 \pm 9.5^\circ$ in PC2 to $173.1 \pm 7.6^\circ$ in PC3, although the
629 inclinations vary more, from $I = -0.2 \pm 14.8^\circ$ in PC2 to $I = -29.4 \pm 15.0^\circ$ in PC5. This overall
630 southeasterly direction cluster differs significantly from the ChRM directions in geographic
631 coordinates from the pillow basalts, that when corrected for the opposite polarity, have a
632 declination difference in geographic coordinates of $\sim 40^\circ$ (Fig. 11B and 12B; Table 4). This

633 suggests that the ChRM directions of the red silts and the pillow lavas do not reflect the same
634 paleomagnetic field, even though they are part of the same stratigraphic sequence, have similar
635 bedding orientations, and are unlikely to be of significantly different age, since the red silts
636 occur at the very base of the sedimentary sequence immediately overlying the pillow lavas. In
637 tectonic coordinates, the magnetic directions of the cherts and pillows are also not antipodal
638 (mean inclination of all PB and all PC sites is -14.4° and 5.9° , respectively, Table 4) and there is a
639 rotation difference: mean declination of all PB and all PC sites is 319.0° and 159.2° , respectively.
640 Between sites PC2 and 3 and the basaltic sections, this angle is approximately 20° . Locality PC5
641 has a bedding strike that is nearly 90° different from the other two PC sections because of local
642 folding and thrusting. The mean paleomagnetic direction obtained from PC5 is also very
643 different to those of localities PC2 and PC3 that have a similar bedding orientation: PC2 and PC3
644 give in tectonic coordinates declinations/inclinations of $164.0 \pm 6.2^\circ / 0.99 \pm 12.4^\circ$ (N=20) and
645 $148.2 \pm 7.6^\circ / 16.5 \pm 14.2^\circ$ (N=9), while PC5 has a declination of $252.4 \pm 25.87^\circ$ and inclination of -
646 $66.6 \pm 12.3^\circ$ (N=12). The fold test of the red silt sections, in any combination, is either negative or
647 inconclusive (Fig. 12C).

648 The magnetization of the pillow basalts in geographic coordinates is profoundly different
649 from that of the remagnetized red siltstones, showing that they were magnetized at different
650 times. In addition, the A95 values of the different PB localities all satisfy the criterion of Deenen
651 et al. (2011, 2014), which suggests that the scatter that we obtained may be explained by
652 paleosecular variation alone, and that paleosecular variation is adequately represented in our
653 sample set. Moreover, the fold test of the basalt sections of PB2 and PB3 gives optimal clustering
654 at $\sim 90\%$ unfolding. We therefore interpret the magnetization of the pillow basalts as primary.
655 Because pillow lavas do not form strictly horizontal bedding and topography may be somewhat
656 rugged during deposition, we consider this as a positive fold test, whereby we note that this test
657 shows that the uncertainty in the bedding tilt correction, and hence in the estimated inclination
658 and paleolatitude, is larger than for normal sediments.

659 Based on the negative fold test of the PC samples, we interpret that the magnetic directions
660 obtained from the red siltstone samples represent a remagnetization of these samples that
661 occurred after folding (i.e., after the late Cretaceous accretion of the Baliojong OPS sequences),
662 but before or during a phase of counterclockwise rotation given the declinations preserved in
663 the sequence that differ significantly from the recent field. Paleomagnetic data from Cenozoic
664 successions have revealed that Borneo underwent $\sim 45^\circ$ of counterclockwise rotation between
665 the late Eocene and early Miocene (Fuller et al., 1999; Advokaat et al., 2018), during which time
666 the Rajang-Crocker accretionary prism formed at the subduction zone that consumed the Proto-
667 South China Sea below the Baliojong section (Hall et al., 2008). It seems plausible that the
668 remagnetization occurred during this time period in a reverse magnetic field, possibly more or

669 less halfway the rotation phase, i.e., sometime in the Oligocene, given the $\sim 15^\circ$
670 counterclockwise rotated overprint direction. Hence, we will not use the paleomagnetic results
671 of the red siltstone samples for further tectonic interpretations.

672 We also tested what the effect on the interpreted inclination would be when the bedding
673 attitude of the oldest overlying red beds would be used to estimate the bedding of the pillow
674 basalts. In all sections, the inclination would become a few degrees shallower, suggesting a
675 somewhat lower latitude. We thus consider the paleolatitudes that we computed using the in
676 situ estimated bedding orientations of the pillows as maximum values.

677 Based on the interpretation that the pillow basalts carry a primary magnetic signal, we use
678 the results in tectonic coordinates for our tectonic analysis. The declination data of the different
679 sections suggest that they all underwent a similar rotation, of about 40° clockwise for a normal,
680 southern hemisphere magnetization, or 140° counterclockwise for a reverse, northern
681 hemisphere magnetization. The pillow basalts of a thrust slice below section 5 formed during
682 the Early Cretaceous (c. 135 Ma; Wang et al., 2023), around which time the magnetic field
683 underwent multiple polarity reversals, which means that the polarity of the magnetic field
684 during magnetization is unknown. In addition, the Baliojong River section is a largely deformed
685 accretionary prism, where large-scale rotations cannot be excluded. Hence, in our tectonic
686 interpretation, we will discuss both the northern and southern hemisphere alternatives of
687 formation of the pillow basalts. The inclination data suggest that the pillow basalts of section B2
688 formed at higher latitudes ($14.7 \pm 4.3^\circ$) than the pillow basalts of section B3 and B4 ($2.5 \pm 3.6^\circ$
689 and $4.5 \pm 3.7^\circ$, respectively), which may indicate that these sequences represent different
690 tectonic nappes that accreted at a different time, whereby B2, with a significantly steeper
691 inclination, may derive from a different nappe that accreted at a later time, because it is
692 structurally deeper.

693

694 **4. Discussion**

695 Our data above suggest that the Baliojong OPS contains nappes that accreted in at least two
696 events at the north Borneo margin. Based on maximum depositional ages of the foreland basin
697 deposits, these events occurred around 92 and 86 Ma, i.e., shortly before the end of Paleo-Pacific
698 subduction inferred from the cessation of arc magmatism in the South China and Indochina
699 regions, and the consequent trapping of the Proto-South China Sea lithosphere (Moss, 1998;
700 Hall and Breitfeld, 2017; Advokaat and Van Hinsbergen, 2023). The interpretation that
701 accretion occurred in at least two events is supported by the differences in geochemistry and
702 heavy mineral composition between the two studied turbidite sections. Our data show that
703 around 86-92 Ma, during the final stages of Paleo-Pacific subduction, an oceanic lithosphere
704 with E-MORB geochemistry was subducting at the north Borneo margin that was then ~ 45 -50

705 Ma old (and currently 135 Ma; Wang et al., 2023). Finally, we show that the ocean floor formed
706 at a paleolatitude ranging from $\sim 14^\circ$ to $\sim 2^\circ$, although we cannot directly infer from the data
707 whether these formed on the northern or southern hemisphere. Placing the reconstruction of
708 Borneo of Advokaat and Van Hinsbergen (2023) in the paleomagnetic reference frame of Vaes
709 et al. (2023) reveals that the latitude of accretion of the OPS sequences at 92-86 Ma was $\sim 3^\circ\text{N}$.
710 This shows that the lithosphere that was underlying the Proto-South China Sea underwent a
711 maximum net motion of up to 17° northwards or 11° southwards in the 45-50 Ma interval
712 between its formation and its accretion in the Late Cretaceous. In the reconstruction of Zahirovic
713 et al. (2014), accretion occurred at $\sim 4^\circ\text{S}$, which would indicate a smaller northward motion of 10° or
714 a larger southward motion of 18°S . As the southward drift scenario does not straightforwardly
715 explain active subduction below the South China margin, we consider the northward drift
716 scenario more likely. We first use this information, combined with constraints from the
717 accretionary prisms of the South China and Palawan margins to re-evaluate the plate kinematic
718 history of the Proto-South China Sea and its motion relative to the Tethyan or Panthalassa plate
719 systems. Next, we re-evaluate previously proposed causes of subduction cessation.

720 The lithosphere that was subducting below the SE China and Indochina margins prior to
721 the late Cretaceous subduction cessation is typically loosely assigned to a Paleo-Pacific plate of
722 the Panthalassa tectonic realm (e.g., Hall and Breitfeld, 2017; Zheng et al., 2019; Zhang et al.,
723 2019). The simplest plate tectonic interpretation is then to infer that this lithosphere formed
724 part of the Izanagi Plate (e.g., Zahirovic et al., 2014; Zhu et al., 2022), whose conjugate spreading
725 records are preserved on the Pacific Plate (Nakanishi et al., 1992). We use our paleomagnetic
726 data to test this hypothesis. To this end, we reconstructed the Proto-South China Sea oceanic
727 crust as part of the Izanagi Plate from 85 Ma (the inferred end of its subduction), backwards in
728 time to 135 Ma, whereby we connect the Panthalassa plate system to the Indo-Atlantic plate
729 system using the reference frames of Torsvik et al. (2019) for the Panthalassa, and of Van der
730 Meer et al. (2010) for the Indo-Atlantic frame prior to 85 Ma, which was shown to best reconcile
731 paleomagnetic and plate kinematic constraints for the eastern Panthalassa-Caribbean realm by
732 Boschman et al. (2019). We then place this connected plate system into the paleomagnetic
733 reference frame of Vaes et al. (2023) to predict the paleolatitude of the Proto-South China Sea
734 for a coordinate coinciding with our sampling locations, using the reconstruction of the Izanagi
735 Plate of Boschman et al. (2021). This results in a predicted paleolatitude that is much farther
736 south ($\sim 30^\circ\text{S}$) than what is obtained from paleomagnetism in this study (Fig. 13). In other
737 words, our data show that the oceanic crust that eventually floored the Proto-South China Sea
738 embayment cannot have been part of the Izanagi Plate but must have been part of a plate with a
739 slower northward motion component than the Izanagi Plate (Fig. 13). Although the

740 paleolongitudinal motion of this plate is unknown, we may infer that it also has a westward
741 motion component relative to Eurasia to satisfy the observation that there was subduction
742 between South China, Indochina, as well as Borneo, whereby Borneo converged with South
743 China (Advokaat and Van Hinsbergen, 2023).

744 Because the Izanagi Plate was moving northwestward at a higher rate than the Proto-South
745 China Sea lithosphere, a subduction zone must have existed between these two plates, whereby
746 Izanagi must have been in a downgoing plate position. A magmatic arc may thus have formed on
747 the eastern boundary of the Proto-South China Sea lithosphere. We infer that the island arc
748 volcanics of c. 100 Ma found in the Cenozoic accretionary prisms of from West Luzon and South
749 Palawan (Pasco et al., 2019; Dycoco et al., 2021), which formed when the Proto-South China Sea
750 eventually subducted, are remains of this intra-oceanic island arc. Interestingly, Van der Meer et
751 al. (2012) inferred such a scenario from lower mantle tomographic images, from which they
752 inferred that in Jurassic to Early Cretaceous time, the Panthalassa plates that surrounded the
753 Pacific plate must have been subducting below an oceanic plate system to the west that was
754 itself separated from the Neotethyan realm by subduction zones. They termed this plate system
755 the 'Pontus Ocean' and named the intervening plate boundary the Telkhinia subduction zone.
756 The relics of 100 Ma arc volcanoes found in the Palawan and west Luzon accretionary prisms
757 may then be fragments of the Telkhinia arc. Because the tomographic resolution shallower than
758 ~2000 km depth was too low for a meaningful interpretation, Van der Meer et al. (2012) were
759 not able to reconstruct when and how the Telkhinia subduction zone came to an end. We infer
760 that this plate boundary eventually evolved to the Philippines-Proto-South China Sea boundary,
761 although detailed kinematic restoration is needed to systematically reconstruct its kinematic
762 history. We infer, however, that the Proto-South China Sea lithosphere was the last remains of
763 the Pontus Ocean and refer to it as the Pontus Plate. The existence of a plate such as the Pontus
764 Plate was previously suggested by Seton et al. (2012), who postulated that a 'Junction Plate'
765 separated from the Panthalassa plates existed between 140 and 70 Ma to account for
766 convergence.

767 We now evaluate why the Pontus Plate did not entirely subduct in the late Cretaceous, but
768 first came to an cessation around 85 Ma, after which it finally subducted between ~40 and 15
769 Ma. There are several models that explain the end of subduction in the circum-Proto-South
770 China Sea region. One model that explains the end of magmatism in SE China and Indochina
771 infers that subduction continued beyond 85 Ma, but retreated southward, which resulted in the
772 opening of the Proto-South China Sea as a back-arc basin analogous to e.g., the Sea of Japan (e.g.,
773 He and Xu, 2012; Li et al., 2012, 2014; Zahirovic et al., 2014; Yan et al., 2017). The model,
774 however, does not explain the presence of a subduction record that ceased at the Borneo
775 margin. Moreover, the ~100 Ma basalts accreted in Palawan during the Oligocene (Dycoco et al.,

776 2021) show that the crust of the Proto-South China Sea formed before the end of South China
777 arc magmatism: the Proto-South China Sea crust can therefore not have formed in a post-85 Ma
778 back-arc basin. Finally, a back-arc basin scenario does not explain how an accretionary prism
779 with Jurassic seamounts was preserved to the north of the Proto-South China Sea in the South
780 China margin (Xu et al., 2022). We conclude that the back-arc basin model does not satisfy the
781 geological data from the accreted OPS sequences in the South China, Palawan, and North Borneo
782 margins.

783 Subduction thus ceased during the Late Cretaceous, even though oceanic crust remained in
784 the foreland. Such a cessation of oceanic subduction may conceptually be explained by the
785 arrival of a mid-oceanic ridge in the subduction zone, as occurred at the continental margin of
786 Antarctica in the south Pacific (Eagles, 2004; Van de Lagemaat et al., 2023), and in the eastern
787 Pacific adjacent to California and Baja California (Atwater, 1989). However, a ridge arrival-
788 scenario is readily excluded for the Proto-South China Sea, because the last subducted oceanic
789 crust that left an accretionary record was at least ~40 Ma old in the Baliojong OPS (this study),
790 and ~60 Ma old in the South China margin (Xu et al., 2022).

791 We therefore propose that subduction ceased because the resistance against subduction of
792 the oceanic lithosphere increased, likely because of enhanced buoyancy. Such a scenario has
793 been proposed before to explain the cessation of subduction below the SE China margin. Hall
794 (2012) and Niu et al. (2015) speculated that subduction may have ceased by the arrival of a
795 microcontinent. While such a scenario may explain subduction cessation, there is no geological
796 evidence for the arrival of a microcontinent in the Cretaceous or its consumption during
797 Eocene-early Miocene subduction below Borneo and Palawan – on the contrary, all accreted
798 records consist of OPS sequences that show no evidence that continental crust was involved in
799 the subduction around the time of subduction cessation.

800 Xu et al. (2022) proposed that the arrival of an oceanic plateau led to the cessation of
801 subduction, and this is a promising explanation. They based their interpretation on the
802 discovery of two Lower Cretaceous seamounts in the south China margin west of Taiwan. The
803 geochemical signatures that we obtained from the pillow basalts of the Baliojong OPS sequence
804 give an E-MORB geochemistry (Fig. 4). According to Xia and Li (2019), oceanic plateau basalts
805 generally have a Transitional-MORB (T-MORB) to E-MORB geochemistry. Samples from the
806 Ontong Java and Caroline plateaus in the West Pacific, for example, display T-MORB to E-MORB
807 geochemical affinities (Zhang et al., 2020). Our results may thus indicate that thickened oceanic
808 lithosphere also arrived at the north Borneo margin shortly before the ~85 Ma of subduction
809 cessation. Interestingly, however, very different ages were obtained from the magmatic rocks
810 that accreted at the Paleo-Pacific margins of South China and SE Asia: ~154 Ma in the north, at
811 the SE China continental margin (Xu et al., 2022), ~135 Ma in NW Borneo (Wang et al., 2023),

812 whereas ~100 Ma arc volcanoes remained in the eastern Proto-South China Sea that eventually
813 ended up in the Palawan and west Luzon accretionary prisms (Pasco et al., 2019; Dycoco et al.,
814 2021).

815 The different ages of accreted mafic rocks suggest that it was perhaps not a single Large
816 Igneous Province like the Ontong-Java Plateau that arrived in the trench, as those generally
817 form within a few million years. Instead, the Proto-South China Sea embayment may have been
818 underlain by a composite plateau that was thickened by multiple magmatic events. In the east,
819 this included the ‘Telkhinia’ arc. Elsewhere, such thickened oceanic crust may have formed in a
820 tectonic setting analogous to the “hotspot-highway” in the Pacific (Jackson et al., 2010) that
821 comprises multiple seamount chains that formed from different hotspot sources in relative
822 proximity, forming a region of thickened oceanic crust with different ages. Alternatively, the
823 different ages may be related to a main event of oceanic plateau formation in the latest Jurassic,
824 with secondary volcanism after the main stage of plateau formation. The Ontong Java Plateau,
825 for example, had a main stage of formation at around 117-118 Ma, but later-stage magmatism
826 also occurred from ~111-108 Ma and at c. 90 Ma (Mahoney et al., 1993; Fitton et al., 2004;
827 Korenaga, 2005; Davidson et al., 2023). The c. 20 Ma age difference in the Pontus Plate
828 volcanoes is therefore not unusual. Regardless of whether it was a true Large Igneous Province
829 or a ‘hotspot-highway’, we suggest that end of subduction at the continental margin
830 surrounding the Pontus Plate in the Proto-South China Sea embayment may have been related
831 to the arrival of thickened oceanic crust, the hypothetical Pontus Plateau (Fig. 14).

832 Even though we infer that thickened crust initially blocked a major and long-lived
833 subduction zone, this fragment of oceanic lithosphere was eventually lost to subduction during
834 the Cenozoic, which suggests that such crust is subductable after all – which must be the case
835 since records of ancient intra-oceanic plateaus are rare (Van Hinsbergen and Schouten, 2021). A
836 similar history has been reconstructed from the Hikurangi Plateau in the SW Pacific. The
837 Hikurangi Plateau is a fragment of the Ontong-Java-Nui Large Igneous Province (Taylor, 2006;
838 Chandler et al., 2012), and its arrival in the New Zealand trench is thought to have caused the
839 shutdown of local subduction at the East Gondwana subduction zone in the Late Cretaceous
840 (e.g., Billen and Stock, 2000; Davy et al., 2008; Van de Lagemaat et al., 2023). Nonetheless, that
841 same plateau is subducting today at the Hikurangi Trench (Collot and Davy, 1998; Timm et al.,
842 2014; Hoernle et al., 2021). It was probably able to stop subduction in the Late Cretaceous
843 because it formed part of a relatively small plate (the Hikurangi Plate; Van de Lagemaat et al.,
844 2023). Today, it forms part of the major Pacific Plate, whose westward motion is forcing the
845 Hikurangi Plate below the Australian Plate at the North Island of New Zealand.

846 Like the Hikurangi Plate, the Pontus Plate was by the Late Cretaceous reduced to a
847 relatively small surface area (Fig. 14). Moreover, it was surrounded by subduction zones. This

848 suggests that the obstruction of the subduction caused by the arrival of an oceanic plateau on
849 the Pontus Plate is geodynamically straightforward. Relative convergence at its eastern
850 boundary that was already being accommodated simply increased to accommodate all Izanagi-
851 Eurasia convergence after the Pontus Plate itself stopped subducting. Subsequently, in the
852 Eocene, when it formed part of the much larger Eurasian Plate, it was ultimately forced to
853 subduct below NW Borneo and the Cagayan arc, likely induced by the 45 Ma pulse of northward
854 motion of the Australian Plate, that triggered a northward motion and counterclockwise
855 rotation of Borneo (Advokaat et al., 2018). And when the Pontus Plate/Proto-South China Sea
856 eventually subducted, it forced the opening of the South China Sea in its wake, in a downgoing
857 plate position. We speculate that eclogitization of the thickened oceanic crust may have
858 generated a slab pull that was so strong that it broke the former accretionary prism at the South
859 China margin to form the South China Sea basin.

860

861 **5. Conclusions**

862 In this paper, we investigated the potential geodynamic causes of enigmatic subduction
863 cessation along the South China Sea margin, which led to the formation of the Proto-South China
864 Sea that from Late Cretaceous to Eocene time intervened Borneo and South China, after which it
865 subducted in the Oligocene-early Miocene. To this end, we studied the youngest accreted rocks
866 that formed at the North Borneo margin during the latest stages of subduction of the Proto-
867 South China Sea lithosphere below northern Borneo, just prior to late Cretaceous subduction
868 cessation. This record is preserved as well-exposed, deformed Ocean Plate Stratigraphy (OPS)
869 remains of the Baliojong River section in Sabah, NW Borneo. We report a detailed analysis of
870 this OPS section. Based on our results from pillow basalt geochemistry, radiolarian
871 biostratigraphy, and detrital zircon geochemistry, geochronology, and provenance, and
872 paleomagnetism we conclude the following:

- 873 1) The Baliojong River exposes different thrust slices of OPS that were likely accreted in at
874 least two events, inferred from the slight variation in basalt geochemistry, sediment
875 provenance and maximum depositional ages, and the different paleolatitudes.
- 876 2) These thrust slices of oceanic crust accreted at different times in the Late Cretaceous,
877 during the final stages of subduction in the Proto-South China Sea embayment, at c. 92
878 and 86 Ma.
- 879 3) The oceanic crust formed at near-equatorial latitudes around 135 Ma. This low latitude
880 excludes that the lithosphere was part of the Izanagi Plate whose spreading history is
881 reconstructed from Pacific Plate anomalies. Instead, the Proto-South China Sea
882 lithosphere was part of a slower NW moving plate below which Izanagi subducted.
883 Remnants of this subduction zone are identified in accretionary prisms on Palawan and

884 western Luzon as ~100 Ma arc volcanic remains. Such a plate system was previously
885 inferred from lower mantle slab remnants (Van der Meer et al., 2012), and following
886 that work, we name the plate to which the Proto-South China Sea lithosphere belonged
887 the Pontus Plate, and the arc remains on its eastern margin the Telkhinia Arc.

888 4) Our geochemical data are consistent with formation of the Baliojong basalts as part of an
889 oceanic plateau. Combined with previously published evidence for seamount accretion
890 in the Late Cretaceous at the South China Sea margin and the Telkhinia arc remains, we
891 infer that subduction cessation resulted from obstruction of the trench induced by
892 thickened, buoyant oceanic lithosphere (the 'Pontus Plateau'), which may have been
893 comparable to the Ontong Java plateau or, alternatively, a series of seamount chains
894 such as the Hotspot Highway of the Central Pacific. Its arrival at the trench caused the
895 end of subduction in the Proto-South China Sea embayment in the Late Cretaceous.

896 5) Final subduction of the Proto-South China Sea lithosphere and the conceptual Pontus
897 Plateau below the Borneo and Palawan margins resulted from convergence between
898 Borneo and South China that was likely induced by an Australia-Eurasia convergence
899 pulse. We speculate that the opening of the South China Sea in the downgoing plate in
900 the wake of the subducting Proto-South China Sea may have resulted from enhanced
901 slab pull when the thickened subducting crust underwent eclogitization.

902

903 **Acknowledgements**

904 SHAvdL and DJJvH were funded by NWO Vici grant 865.17.001 to DJJvH. LC acknowledges
905 funding from the National Natural Science Foundation of China (grant 42106073) and Open
906 Fund of the State Key Laboratory of Marine Geology (Tongji University) (grant MGK202107).
907 We thank Jan van Tongeren and Helen de Waard of the Utrecht University GeoLab for their help
908 with geochemical analysis of the pillow basalts. We thank Tim Breitfeld and an anonymous
909 reviewer for their comments that improved the manuscript.

910

911 **Data statement**

912 Geochemical data of the pillow basalts and geochemical and heavy mineral data of the
913 sandstones is provided as data tables in the main text. Zircon U-Pb data table is provided as
914 Supplementary Table S2. Paleomagnetic data will be made available in the Paleomagnetism.org
915 database (Koymans et al., 2016, 2020), and the MagIC database (Jarboe et al., 2012).

916

917 **References**

- 918 Advokaat, E. L., Marshall, N. T., Li, S., Spakman, W., Krijgsman, W., & van Hinsbergen, D. J. (2018).
919 Cenozoic rotation history of Borneo and Sundaland, SE Asia revealed by paleomagnetism,
920 seismic tomography, and kinematic reconstruction. *Tectonics*, 37(8), 2486-2512.
- 921 Advokaat, E.L., & van Hinsbergen, D.J.J., (2023). Finding Argoland: reconstructing a lost
922 continent in SE Asia. *Gondwana Research*, *accepted pending revision*.
- 923 Atwater, T., 1989. Plate tectonic history of the northeast Pacific and western North America. The
924 eastern Pacific Ocean and Hawaii: Boulder, Colorado, Geological Society of America,
925 *Geology of North America*, v. N: 21-72.
- 926 Aurelio, M. A., Forbes, M. T., Taguibao, K. J. L., Savella, R. B., Bacud, J. A., Franke, D., Pubellier M.,
927 Savva, D., Meresse, F., Steuer, S., & Carranza, C. D. (2014). Middle to Late Cenozoic tectonic
928 events in south and central Palawan (Philippines) and their implications to the evolution
929 of the south-eastern margin of South China Sea: Evidence from onshore structural and
930 offshore seismic data. *Marine and Petroleum Geology*, 58, 658-673.
- 931 Barckhausen, U., Engels, M., Franke, D., Ladage, S., & Pubellier, M. (2014). Evolution of the South
932 China Sea: Revised ages for breakup and seafloor spreading. *Marine and Petroleum*
933 *Geology*, 58, 599-611.
- 934 Bas, M. L., Maitre, R. L., Streckeisen, A., Zanettin, B., & IUGS Subcommittee on the Systematics of
935 Igneous Rocks. (1986). A chemical classification of volcanic rocks based on the total
936 alkali-silica diagram. *Journal of petrology*, 27(3), 745-750.
- 937 Batara, B., & Xu, C. (2022). Evolved magmatic arcs of South Borneo: Insights into Cretaceous slab
938 subduction. *Gondwana Research*, 111, 142-164.
- 939 Billen, M. I., & Stock, J. (2000). Morphology and origin of the Osbourn Trough. *Journal of*
940 *Geophysical Research: Solid Earth*, 105(B6), 13481-13489.
- 941 Berry, K. (2022). A Classopolis “spike” in the Rugubivesiculites Zone of the Kayan Sandstone,
942 western Sarawak, Borneo, suggests a Danian age for these deposits. *Review of*
943 *Palaeobotany and Palynology*, 304, 104728.
- 944 Boschman, L. M., Van der Wiel, E., Flores, K. E., Langereis, C. G., & Van Hinsbergen, D. J. J. (2019).
945 The Caribbean and Farallon plates connected: Constraints from stratigraphy and
946 paleomagnetism of the Nicoya Peninsula, Costa Rica. *Journal of Geophysical Research: Solid*
947 *Earth*, 124(7), 6243-6266.
- 948 Boschman, L. M., Van Hinsbergen, D. J. J., Langereis, C. G., Flores, K. E., Kamp, P. J. J., Kimbrough,
949 D. L., Ueda, H., Van de Lagemaat, S. H. A., Van der Wiel, E. & Spakman, W. (2021).
950 Reconstructing lost plates of the Panthalassa Ocean through paleomagnetic data from
951 circum-Pacific accretionary orogens. *American Journal of Science*, 321(6), 907-954.
- 952 Breitfeld, H. T., Davies, L., Hall, R., Armstrong, R., Forster, M., Lister, G., Thirlwall, M., Grassineau,
953 N., Hennig-Breitfeld, J. & van Hattum, M. W. (2020). Mesozoic Paleo-Pacific subduction
954 beneath SW Borneo: U-Pb geochronology of the Schwaner granitoids and the Pinoh
955 metamorphic group. *Frontiers in Earth Science*, 8, 568715.
- 956 Breitfeld, H. T., Hall, R., Galin, T., & BouDagher-Fadel, M. K. (2018). Unravelling the stratigraphy
957 and sedimentation history of the uppermost Cretaceous to Eocene sediments of the
958 Kuching Zone in West Sarawak (Malaysia), Borneo. *Journal of Asian Earth Sciences*, 160,
959 200-223.
- 960 Breitfeld, H. T., Hall, R., Galin, T., Forster, M. A., & BouDagher-Fadel, M. K. (2017). A Triassic to
961 Cretaceous Sundaland–Pacific subduction margin in West Sarawak,
962 Borneo. *Tectonophysics*, 694, 35-56.
- 963 Briaies, A., Patriat, P., & Tapponnier, P. (1993). Updated interpretation of magnetic anomalies and
964 seafloor spreading stages in the South China Sea: Implications for the Tertiary tectonics of
965 Southeast Asia. *Journal of Geophysical Research: Solid Earth*, 98(B4), 6299-6328.
- 966 Burton-Johnson, A., Macpherson, C. G., Millar, I. L., Whitehouse, M. J., Ottley, C. J., & Nowell, G. M.
967 (2020). A Triassic to Jurassic arc in north Borneo: Geochronology, geochemistry, and
968 genesis of the Segama Valley Felsic Intrusions and the Sabah ophiolite. *Gondwana*
969 *Research*, 84, 229-244.

- 970 Cao, L., Shao, L., Qiao, P., Cui, Y., Zhang, G., & Zhang, X. (2021). Formation and paleogeographic
971 evolution of the Palawan continental terrane along the Southeast Asian margin revealed
972 by detrital fingerprints. *Bulletin*, 133(5-6), 1167-1193.
- 973 Cao, X., Flament, N., Li, S., & Müller, R. D. (2021). Spatio-temporal evolution and dynamic origin
974 of Jurassic-Cretaceous magmatism in the South China Block. *Earth-Science Reviews*, 217,
975 103605.
- 976 Cawood, P.A., Hawkesworth, C.J., Dhuime, B., (2012). Detrital zircon record and tectonic setting.
977 *Geology* 40, 875–878.
- 978 Chandler, M. T., Wessel, P., Taylor, B., Seton, M., Kim, S. S., & Hyeong, K. (2012). Reconstructing
979 Ontong Java Nui: Implications for Pacific absolute plate motion, hotspot drift and true
980 polar wander. *Earth and Planetary Science Letters*, 331, 140-151.
- 981 Collot, J. Y., & Davy, B. (1998). Forearc structures and tectonic regimes at the oblique subduction
982 zone between the Hikurangi Plateau and the southern Kermadec margin. *Journal of*
983 *Geophysical Research: Solid Earth*, 103(B1), 623-650.
- 984 Conand, C., Mouthereau, F., Ganne, J., Lin, A. T. S., Lahfid, A., Daudet, M., Mesalles, L., Giletycz, S., &
985 Bonzani, M. (2020). Strain partitioning and exhumation in oblique Taiwan collision: Role
986 of rift architecture and plate kinematics. *Tectonics*, 39(4), e2019TC005798.
- 987 Coutts, D.S., Matthews, W.A., Hubbard, S.M., (2019). Assessment of widely used methods to
988 derive depositional ages from detrital zircon populations. *Geosci Front* 10, 1421–1435.
- 989 Dankers, P. H. M., & Zijdeveld, J. D. A. (1981). Alternating field demagnetization of rocks, and
990 the problem of gyromagnetic remanence. *Earth and Planetary Science Letters*, 53(1), 89-
991 92.
- 992 Davidson, P. C., Koppers, A. A., Sano, T., & Hanyu, T. (2023). A younger and protracted
993 emplacement of the Ontong Java Plateau. *Science*, 380(6650), 1185-1188.
- 994 Davies, L., Hall, R., & Armstrong, R. (2014). Cretaceous crust in SW Borneo: petrological,
995 geochemical and geochronological constraints from the Schwaner Mountains.
- 996 Davy, B., Hoernle, K., & Werner, R. (2008). Hikurangi Plateau: Crustal structure, rifted formation,
997 and Gondwana subduction history. *Geochemistry, Geophysics, Geosystems*, 9(7).
- 998 De Boer, C. B., & Dekkers, M. J. (1998). Thermomagnetic behaviour of haematite and goethite as
999 a function of grain size in various non-saturating magnetic fields. *Geophysical Journal*
1000 *International*, 133(3), 541-552.
- 1001 Deenen, M. H., Langereis, C. G., van Hinsbergen, D. J., & Biggin, A. J. (2011). Geomagnetic secular
1002 variation and the statistics of palaeomagnetic directions. *Geophysical Journal*
1003 *International*, 186(2), 509-520.
- 1004 Deenen, M. H., Langereis, C. G., van Hinsbergen, D. J., & Biggin, A. J. (2014). Erratum:
1005 Geomagnetic secular variation and the statistics of palaeomagnetic directions. *Geophysical*
1006 *Journal International*, 197(1), 643-643.
- 1007 Dickinson, W.R., Gehrels, G.E., (2009). Use of U-Pb ages of detrital zircons to infer maximum
1008 depositional ages of strata: A test against a Colorado Plateau Mesozoic database. *Earth*
1009 *Planet Sc Lett* 288, 115–125.
- 1010 Dycoco, J. M. A., Payot, B. D., Valera, G. T. V., Labis, F. A. C., Pasco, J. A., Perez, A. D., & Tani, K.
1011 (2021). Juxtaposition of Cenozoic and Mesozoic ophiolites in Palawan island, Philippines:
1012 New insights on the evolution of the Proto-South China Sea. *Tectonophysics*, 819, 229085.
- 1013 Eagles, G. (2004). Tectonic evolution of the Antarctic–Phoenix plate system since 15 Ma. *Earth*
1014 *and Planetary Science Letters*, 217(1-2), 97-109.
- 1015 Faure, M., & Ishida, K. (1990). The Mid-Upper Jurassic olistostrome of the west Philippines: a
1016 distinctive key-marker for the North Palawan block. *Journal of Southeast Asian Earth*
1017 *Sciences*, 4(1), 61-67.
- 1018 Fisher, R. A. (1953). Dispersion on a sphere. *Proceedings of the Royal Society of London. Series A.*
1019 *Mathematical and Physical Sciences*, 217(1130), 295-305.
- 1020 Fitton, J. G., Mahoney, J. J., Wallace, P. J., & Saunders, A. D. (2004). Origin and evolution of the
1021 Ontong Java Plateau: introduction. *Geological Society, London, Special Publications*, 229(1),
1022 1-8.

- 1023 Floyd, P.A., Leveridge, B.E., (1987). Tectonic environment of the Devonian Gramscatho basin,
1024 south Cornwall: framework mode and geochemical evidence from turbiditic sandstones.
1025 *Journal of the Geological Society* 144, 531–542.
- 1026 Fuller, M., Ali, J. R., Moss, S. J., Frost, G. M., Richter, B., & Mahfi, A. (1999). Paleomagnetism of
1027 borneo. *Journal of Asian Earth Sciences*, 17(1-2), 3-24.
- 1028 Gerritsen, D., Vaes, B., & van Hinsbergen, D. J. J. (2022). Influence of data filters on the position
1029 and precision of paleomagnetic poles: what is the optimal sampling
1030 strategy?. *Geochemistry, Geophysics, Geosystems*, 23(4), e2021GC010269.
- 1031 Gibaga, C. R. L., Arcilla, C. A., & Hoang, N. (2020). Volcanic rocks from the Central and Southern
1032 Palawan Ophiolites, Philippines: tectonic and mantle heterogeneity constraints. *Journal of*
1033 *Asian Earth Sciences: X*, 4, 100038.
- 1034 Gradstein, F. M., Ogg, J. G., Schmitz, M. D., & Ogg, G. M. (Eds.). (2020). Geologic time scale 2020.
1035 Elsevier.
- 1036 Grommé, C. S., Wright, T. L., & Peck, D. L. (1969). Magnetic properties and oxidation of iron-
1037 titanium oxide minerals in Alae and Makaopuhi lava lakes, Hawaii. *Journal of Geophysical*
1038 *Research*, 74(22), 5277-5293.
- 1039 Hall, R. (2002). Cenozoic geological and plate tectonic evolution of SE Asia and the SW Pacific:
1040 computer-based reconstructions, model and animations. *Journal of Asian Earth*
1041 *Sciences*, 20(4), 353-431.
- 1042 Hall, R. (2012). Late Jurassic–Cenozoic reconstructions of the Indonesian region and the Indian
1043 Ocean. *Tectonophysics*, 570, 1-41.
- 1044 Hall, R., & Breitfeld, H. T. (2017). Nature and demise of the Proto-South China Sea. *Bulletin of the*
1045 *Geological Society of Malaysia*, 63, 61-67.
- 1046 Hall, R., van Hattum, M. W., & Spakman, W. (2008). Impact of India–Asia collision on SE Asia: the
1047 record in Borneo. *Tectonophysics*, 451(1-4), 366-389.
- 1048 He, Z. Y., & Xu, X. S. (2012). Petrogenesis of the Late Yanshanian mantle-derived intrusions in
1049 southeastern China: response to the geodynamics of Paleo-Pacific plate
1050 subduction. *Chemical Geology*, 328, 208-221.
- 1051 Hennig-Breitfeld, J., Breitfeld, H. T., Hall, R., BouDagher-Fadel, M., & Thirlwall, M. (2019). A new
1052 upper Paleogene to Neogene stratigraphy for Sarawak and Labuan in northwestern
1053 Borneo: Paleogeography of the eastern Sundaland margin. *Earth-science reviews*, 190, 1-
1054 32.
- 1055 Hennig-Breitfeld, J., Breitfeld, H. T., Sang, D. Q., Vinh, M. K., Van Long, T., Thirlwall, M., & Cuong,
1056 T. X. (2021). Ages and character of igneous rocks of the Da Lat Zone in SE Vietnam and
1057 adjacent offshore regions (Cuu Long and Nam Con Son basins). *Journal of Asian Earth*
1058 *Sciences*, 218, 104878.
- 1059 Hennig, J., Breitfeld, H. T., Hall, R., & Nugraha, A. S. (2017). The Mesozoic tectono-magmatic
1060 evolution at the Paleo-Pacific subduction zone in West Borneo. *Gondwana Research*, 48,
1061 292-310.
- 1062 Hieu, P. T., Minh, P., Lei, W. X., Nong, A. T. Q., Kawaguchi, K., & Cuong, T. C. (2022). Zircon U–Pb
1063 geochronology and Sr–Nd–Hf isotopic compositions of the felsic dykes from the Dalat
1064 zone, southern Vietnam: petrogenesis and geological significance. *International Geology*
1065 *Review*, 64(19), 2822-2836.
- 1066 Hinz, K., Block, M., Kudrass, H. R., & Meyer, H. (1994). Structural elements of the Sulu Sea,
1067 Philippines. *AAPG Bulletin (American Association of Petroleum Geologists)*, 78(CONF-
1068 940803-).
- 1069 Ho, C. S. (1986). A synthesis of the geologic evolution of Taiwan. *Tectonophysics*, 125(1-3), 1-16.
- 1070 Hoernle, K., Gill, J., Timm, C., Hauff, F., Werner, R., Garbe-Schönberg, D., & Gutjahr, M. (2021).
1071 Hikurangi Plateau subduction a trigger for Vitiaz arc splitting and Havre Trough opening
1072 (southwestern Pacific). *Geology*, 49(5), 536-540.
- 1073 Holloway, N. H. (1982). North Palawan block, Philippines—its relation to Asian mainland and
1074 role in evolution of South China Sea. *AAPG Bulletin*, 66(9), 1355-1383.

- 1075 Hutchison, C. S. (1996). The 'Rajang accretionary prism' and 'Lupar Line' problem of
 1076 Borneo. *Geological Society, London, Special Publications*, 106(1), 247-261.
- 1077 Hutchison, C.S., Bergman, S.C., Swauger, D.A. and Graves, J.E. (2000). A Miocene collisional belt in
 1078 north Borneo: uplift mechanism and isostatic adjustment quantified by
 1079 thermochronology. *Journal of the Geological Society*, 157, 783-793.
- 1080 Hutchison, C. S. (2005). *Geology of North-West Borneo: Sarawak, Brunei and Sabah*. Elsevier.
- 1081 Isozaki, Y., Aoki, K., Nakama, T., & Yanai, S. (2010). New insight into a subduction-related
 1082 orogen: A reappraisal of the geotectonic framework and evolution of the Japanese
 1083 Islands. *Gondwana Research*, 18(1), 82-105.
- 1084 Isozaki, Y., Maruyama, S., & Furuoka, F. (1990). Accreted oceanic materials in
 1085 Japan. *Tectonophysics*, 181(1-4), 179-205.
- 1086 Jackson, M. G., Hart, S. R., Konter, J. G., Koppers, A. A., Staudigel, H., Kurz, M. D., Blusztajn, J., &
 1087 Sinton, J. M. (2010). Samoan hot spot track on a "hot spot highway": Implications for
 1088 mantle plumes and a deep Samoan mantle source. *Geochemistry, Geophysics,*
 1089 *Geosystems*, 11(12).
- 1090 Jahn, B. M., Chen, P. Y., & Yen, T. P. (1976). Rb-Sr ages of granitic rocks in southeastern China and
 1091 their tectonic significance. *Geological Society of America Bulletin*, 87(5), 763-776.
- 1092 Jahn, B. M., Chi, W. R., & Yui, T. F. (1992). A late Permian formation of Taiwan (marbles from
 1093 Chia-Li well no. 1): Pb-Pb isochron and Sr isotopic evidence, and its regional geological
 1094 significance. *J. Geol. Soc. China*, 35(2), 193-218.
- 1095 Jahn, B. M., Zhou, X. H., & Li, J. L. (1990). Formation and tectonic evolution of southeastern China
 1096 and Taiwan: isotopic and geochemical constraints. *Tectonophysics*, 183(1-4), 145-160.
- 1097 Jarboe, N., Koppers, A., Tauxe, L., Minnett, R. and Constable, C. (2012). The online MagIC
 1098 Database: data archiving, compilation, and visualization for the geomagnetic,
 1099 paleomagnetic and rock magnetic communities, AGU Fall Meeting Abstracts, pp. GP31A-
 1100 1063.
- 1101 Jasin, B. (1991). The Sabah Complex-A lithodemic unit (a new name for the Chert-Spilitite
 1102 Formation and its ultramafic association). *Warta Geologi*, 17, 253-259.
- 1103 Jasin, B. (2000). Significance of Mesozoic radiolarian chert in Sabah and Sarawak. In *Proceedings*
 1104 *Geological Society of Malaysia Annual Conference* (pp. 123-130).
- 1105 Jasin, B., & Said, U. (1999). Significance of Early Jurassic Radiolaria from West Sarawak,
 1106 Malaysia. *Proceedings Geological Society of Malaysia Annual Conference* (pp. 491-502).
- 1107 Jasin, B., & Tongkul, F. (2013). Cretaceous radiolarians from Baliojong ophiolite sequence,
 1108 Sabah, Malaysia. *Journal of Asian Earth Sciences*, 76, 258-265.
- 1109 Jasin, B. (2018). Radiolarian biostratigraphy of Malaysia. *Bulletin of the Geological Society of*
 1110 *Malaysia*, 65, 45-58
- 1111 Ji, W., Lin, W., Faure, M., Chen, Y., Chu, Y., & Xue, Z. (2017). Origin of the Late Jurassic to Early
 1112 Cretaceous peraluminous granitoids in the northeastern Hunan province (middle Yangtze
 1113 region), South China: Geodynamic implications for the Paleo-Pacific subduction. *Journal of*
 1114 *Asian Earth Sciences*, 141, 174-193.
- 1115 Jiang, X. Y., & Li, X. H. (2014). In situ zircon U-Pb and Hf-O isotopic results for ca. 73 Ma granite
 1116 in Hainan Island: Implications for the termination of an Andean-type active continental
 1117 margin in southeast China. *Journal of Asian Earth Sciences*, 82, 32-46.
- 1118 Jiang, Y. H., Wang, G. C., Liu, Z., Ni, C. Y., Qing, L., & Zhang, Q. (2015). Repeated slab advance-
 1119 retreat of the Palaeo-Pacific plate underneath SE China. *International Geology*
 1120 *Review*, 57(4), 472-491.
- 1121 Jochum, K.P., Nohl, U., Herwig, K., Lammel, E., Stoll, B. and Hofmann, A.W., (2005). GeoReM: a
 1122 new geochemical database for reference materials and isotopic standards. *Geostandards*
 1123 *and Geoanalytical Research*, 29(3): 333-338.
- 1124 Kakizaki, Y., Weissert, H., Hasegawa, T., Ishikawa, T., Matsuoka, J., & Kano, A. (2013). Strontium
 1125 and carbon isotope stratigraphy of the Late Jurassic shallow marine limestone in western
 1126 Palaeo-Pacific, northwest Borneo. *Journal of Asian Earth Sciences*, 73, 57-67.

- 1127 Karig, D. E. (1983). Accreted terranes in the northern part of the Philippine
1128 archipelago. *Tectonics*, 2(2), 211-236.
- 1129 Keenan, T. E. (2016). Rapid conversion from spreading to subduction: Structural, geochemical,
1130 and geochronological studies in Palawan, Philippines (*PhD Thesis*, Saint Louis University).
- 1131 Kirschvink, J. (1980). The least-squares line and plane and the analysis of palaeomagnetic
1132 data. *Geophysical Journal International*, 62(3), 699-718.
- 1133 Korenaga, J. (2005). Why did not the Ontong Java Plateau form subaerially?. *Earth and Planetary
1134 Science Letters*, 234(3-4), 385-399.
- 1135 Koymans, M. R., Langereis, C. G., Pastor-Galán, D., & van Hinsbergen, D. J. (2016).
1136 Paleomagnetism.org: An online multi-platform open source environment for
1137 paleomagnetic data analysis.
- 1138 Koymans, M. R., van Hinsbergen, D. J. J., Pastor-Galán, D., Vaes, B., & Langereis, C. G. (2020).
1139 Towards FAIR paleomagnetic data management through Paleomagnetism.org
1140 2.0. *Geochemistry, Geophysics, Geosystems*, 21(2), e2019GC008838.
- 1141 Labis, F. A. C., Payot, B. D., Valera, G. T. V., Pasco, J. A., Dycoco, J. M. A., Tamura, A., Morishita, T., &
1142 Arai, S. (2021). Melt-rock interaction in the subarc mantle: records from the plagioclase
1143 peridotites of the southern Palawan Ophiolite, Philippines. *International Geology
1144 Review*, 63(9), 1067-1089.
- 1145 Lambiase, J. J., Tzong, T. Y., William, A. G., Bidgood, M. D., Brenac, P., & Cullen, A. B. (2008). The
1146 West Crocker formation of northwest Borneo: A Paleogene accretionary prism. In:
1147 Formation and Applications of the Sedimentary Record in Arc Collision Zones, Amy E.
1148 Draut, Peter. D. Clift, David W. Scholl (Eds). GSA Special Papers.
- 1149 Lambiase, J. J., Tzong, T. Y., William, A. G., Bidgood, M. D., Brenac, P., & Cullen, A. B. (2008). The
1150 West Crocker formation of northwest Borneo: A Paleogene accretionary prism.
- 1151 Lapiere, H., Jahn, B. M., Charvet, J., & Yu, Y. W. (1997). Mesozoic felsic arc magmatism and
1152 continental olivine tholeiites in Zhejiang Province and their relationship with the tectonic
1153 activity in southeastern China. *Tectonophysics*, 274(4), 321-338.
- 1154 Larsen, H. C., Mohn, G., Nirrengarten, M., Sun, Z., Stock, J., Jian, Z., ... & Zhong, L. (2018). Rapid
1155 transition from continental breakup to igneous oceanic crust in the South China
1156 Sea. *Nature Geoscience*, 11(10), 782-789.
- 1157 Li, C. F., Xu, X., Lin, J., Sun, Z., Zhu, J., Yao, Y., ... & Zhang, G. L. (2014). Ages and magnetic
1158 structures of the South China Sea constrained by deep tow magnetic surveys and IODP
1159 Expedition 349. *Geochemistry, Geophysics, Geosystems*, 15(12), 4958-4983.
- 1160 Li, H., Ling, M. X., Li, C. Y., Zhang, H., Ding, X., Yang, X. Y., Fan, W. M., Li, Y. L., & Sun, W. D. (2012).
1161 A-type granite belts of two chemical subgroups in central eastern China: Indication of
1162 ridge subduction. *Lithos*, 150, 26-36.
- 1163 Li, J., Zhang, Y., Dong, S., & Johnston, S. T. (2014). Cretaceous tectonic evolution of South China: A
1164 preliminary synthesis. *Earth-Science Reviews*, 134, 98-136.
- 1165 Li, X., Li, J., Yu, X., Wang, C., & Jourdan, F. (2015). ⁴⁰Ar/³⁹Ar ages of seamount trachytes from
1166 the South China Sea and implications for the evolution of the northwestern sub-
1167 basin. *Geoscience Frontiers*, 6(4), 571-577.
- 1168 Li, Z. X., & Li, X. H. (2007). Formation of the 1300-km-wide intracontinental orogen and
1169 postorogenic magmatic province in Mesozoic South China: A flat-slab subduction
1170 model. *Geology*, 35(2), 179-182.
- 1171 Li, Z. X., Li, X. H., Chung, S. L., Lo, C. H., Xu, X., & Li, W. X. (2012). Magmatic switch-on and switch-
1172 off along the South China continental margin since the Permian: Transition from an
1173 Andean-type to a Western Pacific-type plate boundary. *Tectonophysics*, 532, 271-290.
- 1174 Li, Z., Qiu, J. S., & Yang, X. M. (2014). A review of the geochronology and geochemistry of Late
1175 Yanshanian (Cretaceous) plutons along the Fujian coastal area of southeastern China:
1176 Implications for magma evolution related to slab break-off and rollback in the
1177 Cretaceous. *Earth-Science Reviews*, 128, 232-248.
- 1178 Liu, B., Wu, J. H., Li, H., Wu, Q. H., Evans, N. J., Kong, H., & Xi, X. S. (2020). Geochronology,
1179 geochemistry and petrogenesis of the Dengfuxian lamprophyres: Implications for the

- 1180 early Cretaceous tectonic evolution of the South China Block. *Geochemistry*, 80(2),
 1181 125598.
- 1182 Liu, J. X., Wang, S., Wang, X. L., Du, D. H., Xing, G. F., Fu, J. M., Chen, X. & Sun, Z. M. (2020). Refining
 1183 the spatio-temporal distributions of Mesozoic granitoids and volcanic rocks in SE
 1184 China. *Journal of Asian Earth Sciences*, 201, 104503.
- 1185 Longerich, H. P., Jackson, S. E., & Günther, D. (1996). Inter-laboratory note. Laser ablation
 1186 inductively coupled plasma mass spectrometric transient signal data acquisition and
 1187 analyte concentration calculation. *Journal of analytical atomic spectrometry*, 11(9), 899-
 1188 904.
- 1189 Ludwig, K. R. (2003). User's manual for isoplot 3.00, a geochronological toolkit for microsoft
 1190 excel. *Berkeley Geochronol. Cent. Spec. Publ.*, 4, 25-32.
- 1191 Mahoney, J. J., Storey, M., Duncan, R. A., Spencer, K. J., & Pringle, M. (1993). Geochemistry and age
 1192 of the Ontong Java Plateau. *The mesozoic Pacific: Geology, tectonics, and volcanism*, 77,
 1193 McLennan, S.M., Hemming, S., McDaniel, D.K., Hanson, G.N., (1993). Geochemical approaches to
 1194 sedimentation, provenance, and tectonics, in: Johnsson, M.J., Basu, A. (Eds.), Processes
 1195 Controlling the Composition of Clastic Sediments, Geological Society of America Special
 1196 Paper. Geological Society of America, Colorado, pp. 21–40.
- 1197 Metcalfe, I. (1985). Lower Permian conodonts from the Terbat formation, Sarawak. *Warta Geologi* 11,
 1198 1-4.
- 1199 Morley, C. K. (2016). Major unconformities/termination of extension events and associated
 1200 surfaces in the South China Seas: Review and implications for tectonic
 1201 development. *Journal of Asian Earth Sciences*, 120, 62-86.
- 1202 Moss, S. J. (1998). Embaluh Group turbidites in Kalimantan: evolution of a remnant oceanic
 1203 basin in Borneo during the Late Cretaceous to Palaeogene. *Journal of the Geological
 1204 Society*, 155(3), 509-524.
- 1205 Mullender, T. A. T., Van Velzen, A. J., & Dekkers, M. J. (1993). Continuous drift correction and
 1206 separate identification of ferrimagnetic and paramagnetic contributions in
 1207 thermomagnetic runs. *Geophysical Journal International*, 114(3), 663-672.
- 1208 Mullender, T. A., Frederichs, T., Hilgenfeldt, C., de Groot, L. V., Fabian, K., & Dekkers, M. J. (2016).
 1209 Automated paleomagnetic and rock magnetic data acquisition with an in-line horizontal
 1210 “2 G” system. *Geochemistry, Geophysics, Geosystems*, 17(9), 3546-3559.
- 1211 Muller, C. (1991). Biostratigraphy and geological evolution of the Sulu Sea and surrounding
 1212 area. In *Proceedings of the Ocean Drilling Program, Scientific Results* (Vol. 124, pp. 121-
 1213 131). Ocean Drilling Program.
- 1214 Nakanishi, M., Tamaki, K., & Kobayashi, K. (1992). Magnetic anomaly lineations from Late
 1215 Jurassic to Early Cretaceous in the west-central Pacific Ocean. *Geophysical Journal
 1216 International*, 109(3), 701-719.
- 1217 Nguyen, T. T. B., Satir, M., Siebel, W., & Chen, F. (2004). Granitoids in the Dalat zone, southern
 1218 Vietnam: age constraints on magmatism and regional geological
 1219 implications. *International Journal of Earth Sciences*, 93, 329-340.
- 1220 Niu, Y., Liu, Y., Xue, Q., Shao, F., Chen, S., Duan, M., Guo, P., Gong, H., Hu, Y., Hu, Z., Kong, J., Li, J.,
 1221 Liu, J., Sun, P., Sun, W., Ye, L, Xiao, Y. & Zhang, Y. (2015). Exotic origin of the Chinese
 1222 continental shelf: new insights into the tectonic evolution of the western Pacific and
 1223 eastern China since the Mesozoic. *Science Bulletin*, 60(18), 1598-1616.
- 1224 NOAA National Centers for Environmental Information. 2022: ETOPO 2022 15 Arc-Second
 1225 Global Relief Model. NOAA National Centers for Environmental Information.
- 1226 Nong, A. T., Hauzenberger, C. A., Gallhofer, D., & Dinh, S. Q. (2021). Geochemistry and zircon UPb
 1227 geochronology of Late Mesozoic igneous rocks from SW Vietnam–SE Cambodia:
 1228 Implications for episodic magmatism in the context of the Paleo-Pacific
 1229 subduction. *Lithos*, 390, 106101.
- 1230 Nong, A. T., Hauzenberger, C. A., Gallhofer, D., Skrzypek, E., & Dinh, S. Q. (2022). Geochemical and
 1231 zircon U-Pb geochronological constraints on late mesozoic Paleo-Pacific subduction-
 1232 related volcanism in southern Vietnam. *Mineralogy and Petrology*, 116(5), 349-368.

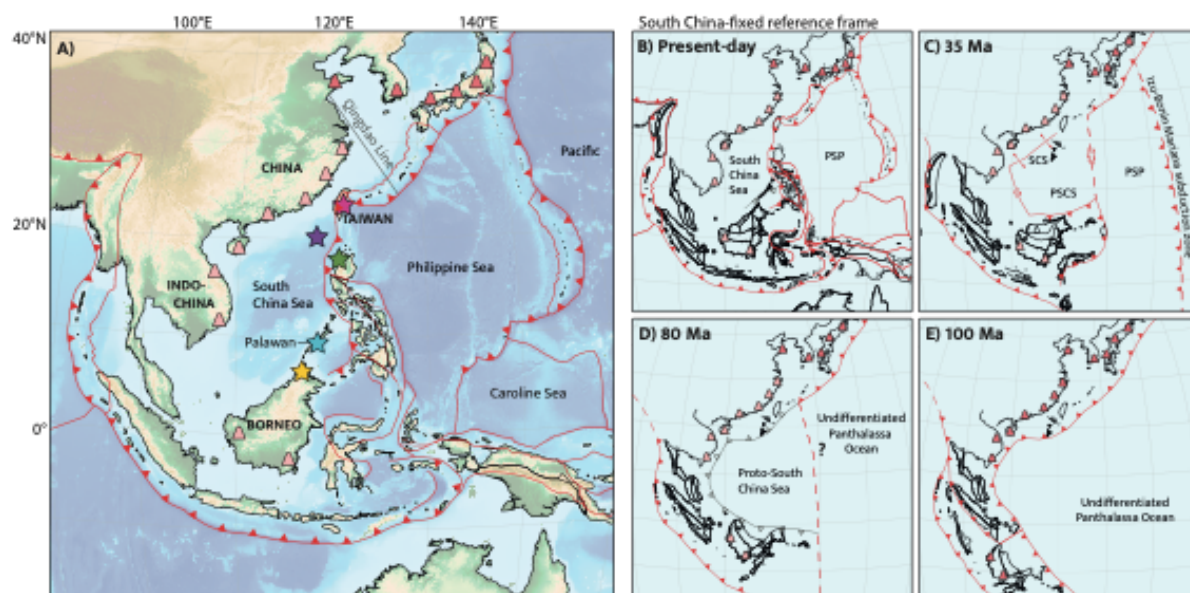
- 1233 O'Dogherty, L. 1994. Biochronology and Plaeontology of Mid-Cretaceous Radiolarians from
1234 Northern Apennines (Italy) and Betic Cordillera (Spain). *Memoires de Geologie*
1235 (Lausanne). 21, 1-413.
- 1236 Pasco, J. A., Dycoco, J. M. A., Valera, G. T. V., Payot, B. D., Pillejera, J. D. B., Uy, F. A. A. E., Armada, L.
1237 T., & Dimalanta, C. B. (2019). Petrogenesis of ultramafic-mafic clasts in the Dos Hermanos
1238 Mélange, Ilocos Norte: insights to the evolution of western Luzon, Philippines. *Journal of*
1239 *Asian Earth Sciences*, 184, 104004.
- 1240 Pearce, J. A. (2008). Geochemical fingerprinting of oceanic basalts with applications to ophiolite
1241 classification and the search for Archean oceanic crust. *Lithos*, 100(1-4), 14-48.
- 1242 Pessagno, E.A. & Newport, R.L. (1972). A technique for extracting Radiolaria from Radiolarian
1243 chert. *Micropaleontology* 18(2), 231-234.
- 1244 Qian, X., Yu, Y., Wang, Y., Gan, C., Zhang, Y., & Asis, J. B. (2022). Late Cretaceous Nature of SW
1245 Borneo and Paleo-Pacific Subduction: New Insights from the Granitoids in the Schwaner
1246 Mountains. *Lithosphere*, 2022(1), 8483732.
- 1247 Queaño, K. L., Marquez, E. J., Dimalanta, C. B., Aitchison, J. C., Ali, J. R., & Yumul Jr, G. P. (2017).
1248 Mesozoic radiolarian faunas from the northwest Ilocos Region, Luzon, Philippines and
1249 their tectonic significance. *Island Arc*, 26(4), e12195.
- 1250 Rahim, A. R., Konjing, Z., Asis, J., Jalil, N. A., Muhamad, A. J., Ibrahim, N., Munif Koraini, A., Che
1251 Kob, R., Mazlan, H., & Tjia, H. D. (2017). Tectonostratigraphic terranes of Kudat Peninsula,
1252 Sabah.
- 1253 Rinke-Hardekopf, L., Dashtgard, S.E., Huang, C., Gibson, H.D., (2021). Application of grouped
1254 detrital zircon analyses to determine provenance and closely approximate true
1255 depositional age: Early Cretaceous McMurray-Clearwater succession, Canada.
1256 *Geoscience Frontiers* 12, 877–892.
- 1257 Rollinson, H. R., Rollinson, H., & Pease, V. (2021). *Using geochemical data: To understand*
1258 *geological processes*. Cambridge University Press.
- 1259 Roser, B., Korsch, R., (1988). Provenance signatures of sandstone-mudstone suites determined
1260 using discriminant function analysis of major-element data. *Chemical Geology* 67, 119–
1261 139.
- 1262 Rudnick, R L, Gao, S., (2003). Composition of the continental crust, in: Rudnick, Roberta L. (Ed.),
1263 *Treatise in Geochemistry Vol. 3, The Crust*. Elsevier, Oxford, pp. 1–64.
- 1264 Sanfilippo, A. & Riedel, W.R. (1985). Cretaceous Radiolaria. In. Bolli, H.M., Saunders, J.B. & Perch-
1265 Nielsen, K. (Ed.). *Plankton Stratigraphy*, 631-712. New York: Cambridge University Press.
- 1266 Schlüter, H. U., Hinz, K., & Block, M. (1996). Tectono-stratigraphic terranes and detachment
1267 faulting of the South China Sea and Sulu Sea. *Marine Geology*, 130(1-2), 39-78.
- 1268 Schmidtke, E. A., Fuller, M. D., & Haston, R. B. (1990). Paleomagnetic data from Sarawak,
1269 Malaysian Borneo, and the late Mesozoic and Cenozoic tectonics of
1270 Sundaland. *Tectonics*, 9(1), 123-140.
- 1271 Shao, L., Cao, L., Qiao, P., Zhang, X., Li, Q., & van Hinsbergen, D. J. (2017). Cretaceous–Eocene
1272 provenance connections between the Palawan Continental Terrane and the northern
1273 South China Sea margin. *Earth and Planetary Science Letters*, 477, 97-107.
- 1274 Shellnutt, J. G., Lan, C. Y., Van Long, T., Usuki, T., Yang, H. J., Mertzman, S. A., Iizuka, Y., Chung, S.L.,
1275 Wang, K.L., & Hsu, W. Y. (2013). Formation of Cretaceous Cordilleran and post-orogenic
1276 granites and their microgranular enclaves from the Dalat zone, southern Vietnam:
1277 Tectonic implications for the evolution of Southeast Asia. *Lithos*, 182, 229-241.
- 1278 Shellnutt, J. G., Ma, G. S. K., Chan, J. S. L., Wong, J. P. M., & Wang, K. L. (2023). Early Cretaceous
1279 volcanic-arc magmatism in the Dalat-Kratie Fold Belt of eastern Cambodia: implications
1280 for the lithotectonic evolution of the Indochina terrane. *Frontiers in Earth Science*, 11,
1281 1110568.
- 1282 Steuer, S., Franke, D., Meresse, F., Savva, D., Pubellier, M., Auxietre, J. L., & Aurelio, M. (2013).
1283 Time constraints on the evolution of southern Palawan Island, Philippines from onshore
1284 and offshore correlation of Miocene limestones. *Journal of Asian Earth Sciences*, 76, 412-
1285 427.

- 1286 Suggate, S. M., Cottam, M. A., Hall, R., Sevastjanova, I., Forster, M. A., White, L. T., Armstrong, R. A.,
1287 Carter, A., & Mojares, E. (2014). South China continental margin signature for sandstones
1288 and granites from Palawan, Philippines. *Gondwana Research*, 26(2), 699-718.
- 1289 Sun, P., Guo, P., & Niu, Y. (2021). Eastern China continental lithosphere thinning is a
1290 consequence of Paleo-Pacific plate subduction: A review and new perspectives. *Earth-*
1291 *Science Reviews*, 218, 103680.
- 1292 Sun, S.-S., McDonough, W.F., (1989). Chemical and isotopic systematics of oceanic basalts:
1293 implications for mantle composition and processes. Geological Society, London, Special
1294 Publications 42, 313-345.
- 1295 Tauxe, L., & Watson, G. S. (1994). The fold test: an eigen analysis approach. *Earth and Planetary*
1296 *Science Letters*, 122(3-4), 331-341.
- 1297 Tauxe, L., with contributions from Butler, R.F., Van der Voo, R., and Banerjee, S.K., (2010).
1298 *Essentials of Paleomagnetism*, University of California Press
- 1299 Taylor, B., & Hayes, D. E. (1983). Origin and history of the South China Sea basin. *Washington DC*
1300 *American geophysical union geophysical monograph series*, 27, 23-56.
- 1301 Taylor, B. (2006). The single largest oceanic plateau: Ontong Java–Manihiki–Hikurangi. *Earth*
1302 *and Planetary Science Letters*, 241(3-4), 372-380.
- 1303 Thurow, J. (1988). Cretaceous radiolarians of the North Atlantic Ocean: ODP Leg 103 (Site 638,
1304 640 and 641) and DSDP Legs 93 (Site 603) and 47B (Site 398). In. Boillot, G., Winterer,
1305 E.L. et al. (Ed.). Proceedings of the Ocean Drilling Program, Scientific Result 103, 379-418.
1306 Texas, College Station.
- 1307 Thuy, N. T. B., Satir, M., Siebel, W., Vennemann, T., & Van Long, T. (2004). Geochemical and
1308 isotopic constraints on the petrogenesis of granitoids from the Dalat zone, southern
1309 Vietnam. *Journal of Asian Earth Sciences*, 23(4), 467-482.
- 1310 Timm, C., Davy, B., Haase, K., Hoernle, K. A., Graham, I. J., De Ronde, C. E., ... & Gamble, J. A.
1311 (2014). Subduction of the oceanic Hikurangi Plateau and its impact on the Kermadec
1312 arc. *Nature Communications*, 5(1), 4923.
- 1313 Vaes, B., Van Hinsbergen, D. J. J., Van de Lagemaat, S. H. A., Van der Wiel, E., Lom, N., Advokaat, E.,
1314 ... & Langereis, C. (2023). A global apparent polar wander path for the last 320 Ma
1315 calculated from site-level paleomagnetic data. *Earth-Science Reviews*, 104547.
- 1316 Van de Lagemaat, S. H. A., Kamp, P. J. J., Boschman, L. M., & Van Hinsbergen, D. J. J. (2023).
1317 Reconciling the Cretaceous breakup and demise of the Phoenix Plate with East Gondwana
1318 orogenesis in New Zealand. *Earth-Science Reviews*, 104276.
- 1319 Van Der Meer, D. G., Spakman, W., Van Hinsbergen, D. J., Amaru, M. L., & Torsvik, T. H. (2010).
1320 Towards absolute plate motions constrained by lower-mantle slab remnants. *Nature*
1321 *Geoscience*, 3(1), 36-40.
- 1322 Van der Meer, D. G., Torsvik, T. H., Spakman, W., Van Hinsbergen, D. J. J., & Amaru, M. L. (2012).
1323 Intra-Panthalassa Ocean subduction zones revealed by fossil arcs and mantle
1324 structure. *Nature Geoscience*, 5(3), 215-219.
- 1325 Van Hattum, M. W. A., Hall, R., Pickard, A. L., & Nichols, G. J. (2013). Provenance and
1326 geochronology of Cenozoic
- 1327 Van Hattum, M. W., Hall, R., Pickard, A. L., & Nichols, G. J. (2006). Southeast Asian sediments not
1328 from Asia: Provenance and geochronology of north Borneo sandstones. *Geology*, 34(7),
1329 589-592. sandstones of northern Borneo. *Journal of Asian Earth Sciences*, 76, 266-282.
- 1330 Van Hinsbergen, D. J. J., & Schouten, T. L. (2021). Deciphering paleogeography from orogenic
1331 architecture: constructing orogens in a future supercontinent as thought
1332 experiment. *American Journal of Science*, 321(6), 955-1031.233-261.
- 1333 Van Hinsbergen, D.J.J., Dekkers, M.J., Bozkurt, E. and Koopman, M., (2010). Exhumation with a
1334 twist: Paleomagnetic constraints on the evolution of the Menderes metamorphic core
1335 complex, western Turkey. *Tectonics*, 29(3).
- 1336 Vermeesch, P. (2021). Maximum depositional age estimation revisited. *Geoscience*
1337 *Frontiers*, 12(2), 843-850.

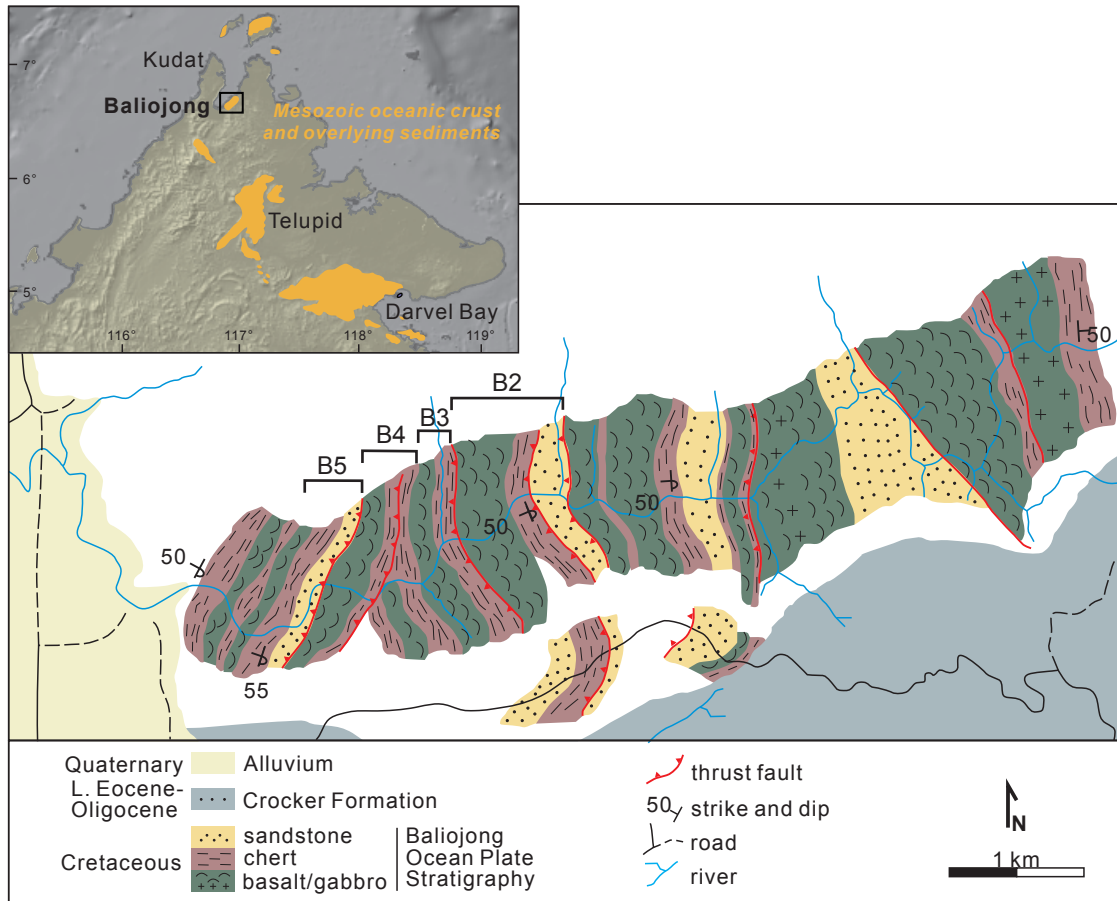
- 1338 Vishnevskaya, V.S. (1993). Jurassic and Cretaceous radiolarian biostratigraphy in Russia. In.
 1339 Blueford, J. & Murchey, B. (Eds.). Radiolarian of giant and subgiant fields in Asia, 175-200.
 1340 Micropaleontology special publ. 6.
- 1341 Waight, T., Fyhn, M. B., Thomsen, T. B., Van Tri, T., Nielsen, L. H., Abatzis, I., & Frei, D. (2021).
 1342 Permian to Cretaceous granites and felsic volcanics from SW Vietnam and S Cambodia:
 1343 Implications for tectonic development of Indochina. *Journal of Asian Earth Sciences*, 219,
 1344 104902.
- 1345 Wang, K. L., Lo, Y. M., Chung, S. L., Lo, C. H., Hsu, S. K., Yang, H. J., & Shinjo, R. (2012). Age and
 1346 Geochemical Features of Dredged Basalts from Offshore SW Taiwan: The Coincidence of
 1347 Intra-Plate Magmatism with the Spreading South China Sea. *Terrestrial, Atmospheric &
 1348 Oceanic Sciences*, 23(6).
- 1349 Wang, Y., Qian, X., Asis, J. B., Cawood, P. A., Wu, S., Zhang, Y., Wu, S., Zhang, Y., Feng, Q., & Lu, X.
 1350 (2023). "Where, when and why" for the arc-trench gap from Mesozoic Paleo-Pacific
 1351 subduction zone: Sabah Triassic-Cretaceous igneous records in East Borneo. *Gondwana
 1352 Research*, 117, 117-138.
- 1353 Wang, Y., Zhang, A., Qian, X., Asis, J. B., Feng, Q., Gan, C., Zhang, Y., Cawood, P. A., Wang, W., &
 1354 Zhang, P. (2021). Cretaceous Kuching accretionary orogenesis in Malaysia Sarawak:
 1355 Geochronological and geochemical constraints from mafic and sedimentary
 1356 rocks. *Lithos*, 400, 106425.
- 1357 Wolfart, R., Čeppek, P., Gramann, F., Kemper, E., & Porth, H. (1986). Stratigraphy of Palawan
 1358 Island, Philippines. *Newsletters on Stratigraphy*, 16: 19-48.
- 1359 Wu, J. and Suppe, J. (2018). Proto-South China Sea plate tectonics using subducted slab
 1360 constraints from tomography. *Journal of Earth Science*, 29: 1304-1318.
- 1361 Wu, Z., Zhu, W., Shao, L., & Xu, C. (2016). Sedimentary facies and the rifting process during the
 1362 late Cretaceous to early Oligocene in the northern continental margin, South China
 1363 Sea. *Interpretation*, 4(3), SP33-SP45.
- 1364 Xia, L., & Li, X. (2019). Basalt geochemistry as a diagnostic indicator of tectonic
 1365 setting. *Gondwana Research*, 65, 43-67.
- 1366 Xu, X., Dong, C., Li, W., & Zhou, X. (1999). Late Mesozoic intrusive complexes in the coastal area
 1367 of Fujian, SE China: the significance of the gabbro-diorite-granite
 1368 association. *Lithos*, 46(2), 299-315.
- 1369 Xu, Y., Yan, Q., Shi, X., Jichao, Y., Deng, X., Xu, W., & Jing, C. (2022). Discovery of Late Mesozoic
 1370 volcanic seamounts at the ocean-continent transition zone in the Northeastern margin of
 1371 South China Sea and its tectonic implication. *Gondwana Research*.
- 1372 Xu, Y., Yang, Y., Yu, H., Gao, W., Gao, X., Liu, B., Tian, C., Yang, J., & Zhang, W. (2020). Geochemistry
 1373 and petrogenesis of volcanic rocks from the continent-ocean transition zone in northern
 1374 South China Sea and their tectonic implications. *Journal of Ocean University of
 1375 China*, 19(5), 1051-1061.
- 1376 Yan, Q., Metcalfe, I., & Shi, X. (2017). U-Pb isotope geochronology and geochemistry of granites
 1377 from Hainan Island (northern South China Sea margin): Constraints on late Paleozoic-
 1378 Mesozoic tectonic evolution. *Gondwana Research*, 49, 333-349.
- 1379 Ye, Q., Mei, L., Shi, H., Camanni, G., Shu, Y., Wu, J., Yu, L., Deng, P. & Li, G. (2018). The Late
 1380 Cretaceous tectonic evolution of the South China Sea area: An overview, and new
 1381 perspectives from 3D seismic reflection data. *Earth-science reviews*, 187, 186-204.
- 1382 Yui, T. F., Maki, K., Lan, C. Y., Hirata, T., Chu, H. T., Kon, Y., Yokoyama, T. D., Jahn, B. M., & Ernst, W.
 1383 G. (2012). Detrital zircons from the Tananao metamorphic complex of Taiwan:
 1384 Implications for sediment provenance and Mesozoic tectonics. *Tectonophysics*, 541, 31-42.
- 1385 Yui, T. F., Okamoto, K., Usuki, T., Lan, C. Y., Chu, H. T., & Liou, J. G. (2009). Late Triassic-Late
 1386 Cretaceous accretion/subduction in the Taiwan region along the eastern margin of South
 1387 China—evidence from zircon SHRIMP dating. *International Geology Review*, 51(4), 304-328.
- 1388 Yumul Jr, G. P., Dimalanta, C. B., Gabo-Ratio, J. A. S., Queaño, K. L., Armada, L. T., Padrones, J. T.,
 1389 Faustino-Eslava, D. V., Payot, B. D., & Marquez, E. J. (2020). Mesozoic rock suites along

- 1390 western Philippines: Exposed Proto-South China Sea fragments?. *Journal of Asian Earth*
1391 *Sciences*: X, 4, 100031.
- 1392 Zahirovic, S., Seton, M., & Müller, R. D. (2014). The cretaceous and cenozoic tectonic evolution of
1393 Southeast Asia. *Solid Earth*, 5(1), 227-273.
- 1394 Zamoras, L. R., Montes, M. G. A., Queano, K. L., Marquez, E. J., Dimalanta, C. B., Gabo, J. A. S., &
1395 Yumul Jr, G. P. (2008). Buruanga peninsula and Antique Range: two contrasting terranes
1396 in Northwest Panay, Philippines featuring an arc–continent collision zone. *Island Arc*,
1397 17(4), 443-457.
- 1398 Zamoras, L. R., & Matsuoka, A. (2001). The Malampaya Sound Group in the Calamian Islands,
1399 North Palawan Block (Philippines). *The Journal of the Geological Society of Japan*, 107(5),
1400 XI-XII.
- 1401 Zamoras, L. R., & Matsuoka, A. (2004). Accretion and postaccretion tectonics of the Calamian
1402 Islands, North Palawan block, Philippines. *Island Arc*, 13(4), 506-519.
- 1403 Zhang, A., Asis, J. B., Fang, X., Li, H., Omang, S. A., Chen, M., Fang, Q., Li, D., & Peng, T. (2022). Late
1404 Cretaceous fore–arc spreading in the northern Kuching Zone of West Borneo, SE Asia:
1405 Constraints from the Pakong Mafic Complex. *Journal of Asian Earth Sciences*, 230, 105189.
- 1406 Zhang, B., Guo, F., Zhang, X., Wu, Y., Wang, G., & Zhao, L. (2019). Early Cretaceous subduction of
1407 Paleo-Pacific Ocean in the coastal region of SE China: Petrological and geochemical
1408 constraints from the mafic intrusions. *Lithos*, 334, 8-24.
- 1409 Zhang, G., Zhang, J., Wang, S., & Zhao, J. (2020). Geochemical and chronological constraints on
1410 the mantle plume origin of the Caroline Plateau. *Chemical Geology*, 540, 119566.
- 1411 Zhang, X., Pease, V., Skogseid, J., Wohlgenuth-Ueberwasser, C., 2015. Reconstruction of tectonic
1412 events on the northern Eurasia margin of the Arctic, from U-Pb detrital zircon
1413 provenance investigations of late Paleozoic to Mesozoic sandstones in southern Taimyr
1414 Peninsula. *Geological Society of America Bulletin* B31241.1.
- 1415 Zhao, Q., Yan, Y., Zhu, Z., Carter, A., Clift, P. D., Hassan, M. H. A., Yao, D., & Aziz, J. H. A. (2021).
1416 Provenance study of the Lubok Antu Melange from the Lupar valley, West Sarawak,
1417 Borneo: Implications for the closure of eastern Meso-Tethys?. *Chemical Geology*, 581,
1418 120415.
- 1419 Zheng, H., Sun, X., Wang, P., Chen, W., & Yue, J. (2019). Mesozoic tectonic evolution of the Proto-
1420 South China Sea: A perspective from radiolarian paleobiogeography. *Journal of Asian*
1421 *Earth Sciences*, 179, 37-55.
- 1422 Zhou, D., Wang, W., Wang, J., Pang, X., Cai, D., & Sun, Z. (2006). Mesozoic subduction-accretion
1423 zone in northeastern South China Sea inferred from geophysical interpretations. *Science*
1424 *China. Earth Sciences*, 49(5), 471.
- 1425 Zhou, X. M., & Li, W. X. (2000). Origin of Late Mesozoic igneous rocks in Southeastern China:
1426 implications for lithosphere subduction and underplating of mafic
1427 magmas. *Tectonophysics*, 326(3-4), 269-287.
- 1428 Zhou, X., Sun, T., Shen, W., Shu, L., & Niu, Y. (2006). Petrogenesis of Mesozoic granitoids and
1429 volcanic rocks in South China: a response to tectonic evolution. *Episodes Journal of*
1430 *International Geoscience*, 29(1), 26-33.
- 1431 Zhu, J., Li, S., Jia, Y., Zhang, S., Chen, X., Chen, R., Suo, Y., Cao, X., Jia, Z., Ou, X., Liu, J., Wang, P., &
1432 Zhou, J. (2022). Links of high velocity anomalies in the mantle to the Proto-South China
1433 Sea slabs: Tomography-based review and perspective. *Earth-Science Reviews*, 231,
1434 104074.
- 1435 Zhu, W., Xie, X., Wang, Z., Zhang, D., Zhang, C., Cao, L., & Shao, L. (2017). New insights on the
1436 origin of the basement of the Xisha Uplift, South China Sea. *Science China Earth*
1437 *Sciences*, 60, 2214-2222.
- 1438 Zijdeveld, J.D.A. (1967): A.C. demagnetization of rocks: analysis of results. In D.W. Collinson,
1439 K.M. Crees and S.K. Runcorn (Eds.) *Methods in Paleomagnetism* (pp. 254-286). Elsevier,
1440 Amsterdam.

1441 **Figures**
 1442



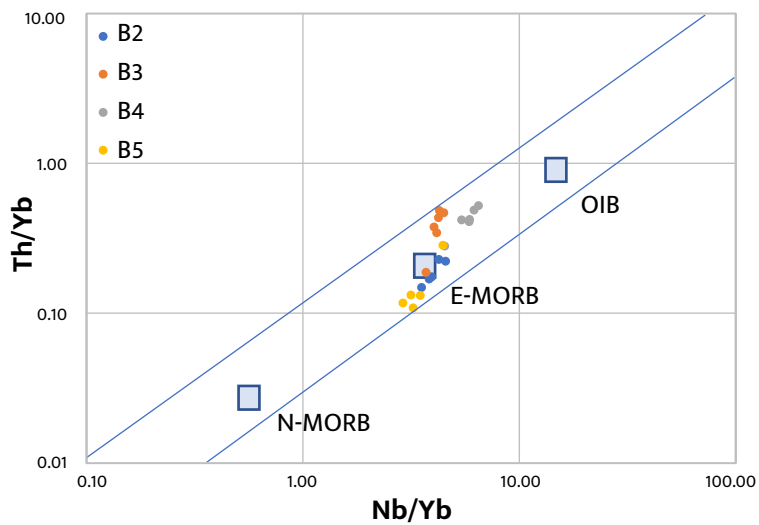
1443 **Figure 1: A)** Present-day map of the (proto-)South China region. Stars mark locations of
 1444 geological data from the Proto-South China Sea: Yellow: Baliojong River (this study); Blue: South
 1445 Palawan Ophiolite; Green: Dos Hermanos Mélange; Purple: Accreted seamounts; Pink: Tailuko
 1446 Belt. Dark pink cones indicate active arc magmatism, light pink cones indicate extinct arc
 1447 magmatism. Arc magmatism has been continuously active northeast of the Qingdao Line,
 1448 whereas it went extinct in the Late Mesozoic to the southwest of this line. **B-E)** Simplified Late
 1449 Mesozoic - Cenozoic tectonic evolution of the proto-South China region, based on the
 1450 reconstruction of Advokaat and Van Hinsbergen (2023), in a South China-fixed reference frame.
 1451 Active plate boundaries are shown in red, former plate boundaries in gray. Dark pink cones
 1452 indicate active arc magmatism, light pink cones indicate extinct arc magmatism. Background
 1453 image is ETOPO 2022 15 Arc-Second Global Relief Model. (NOAA National Centers for
 1454 Environmental Information, 2022).
 1455
 1456



1457
 1458 **Figure 2:** Geological map of the OPS sections of the Baliojong River showing the sampled
 1459 sections (based on Jasin and Tongkul, 2013). Inset: Generalized geological map of Sabah,
 1460 showing the distribution of Mesozoic ophiolite and OPS exposures.



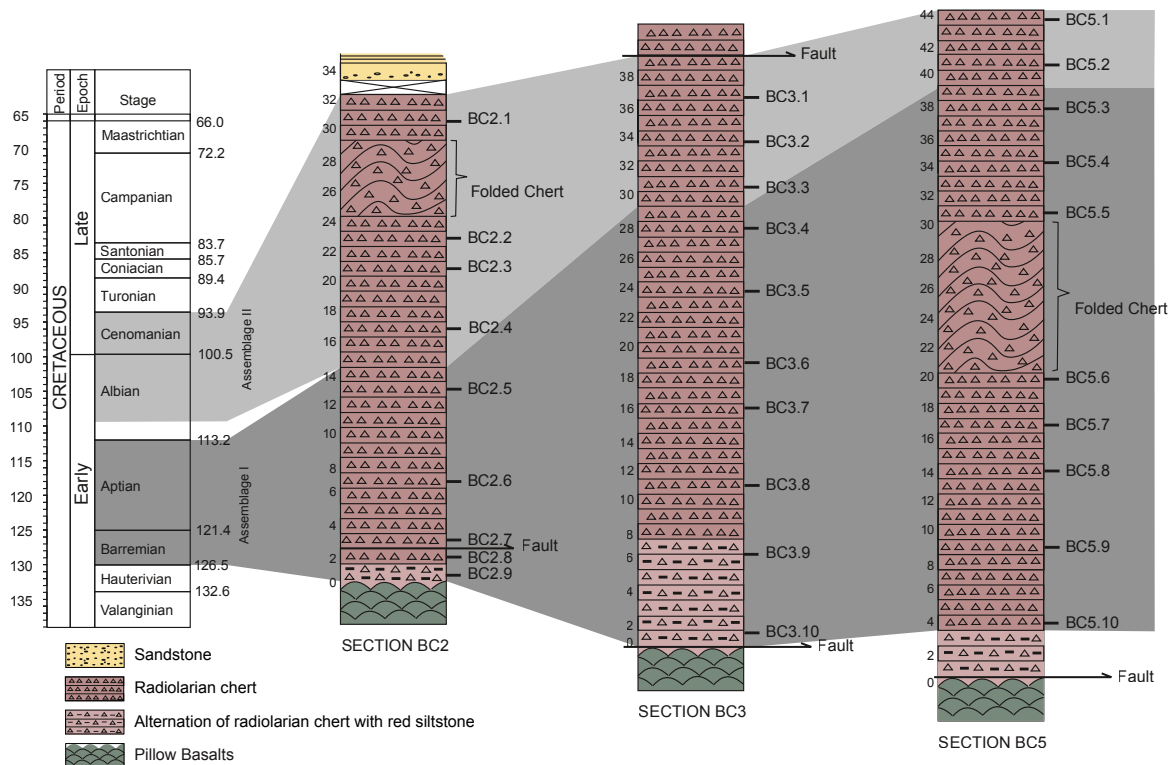
1461
 1462 **Figure 3:** Field photos from the Baliojong River OPS: A) Sandstone turbidite; B) Overturned
 1463 contact (highlighted with yellow line) between pillow basalts and radiolarian cherts; C)
 1464 Rhythmic alternation between radiolarian chert and red cherty siltstone; D) Pillow basalts.



1465

1466 **Figure 4:** Th/Yb versus Nb/Yb diagram of the Baliojong River pillow basalt samples.

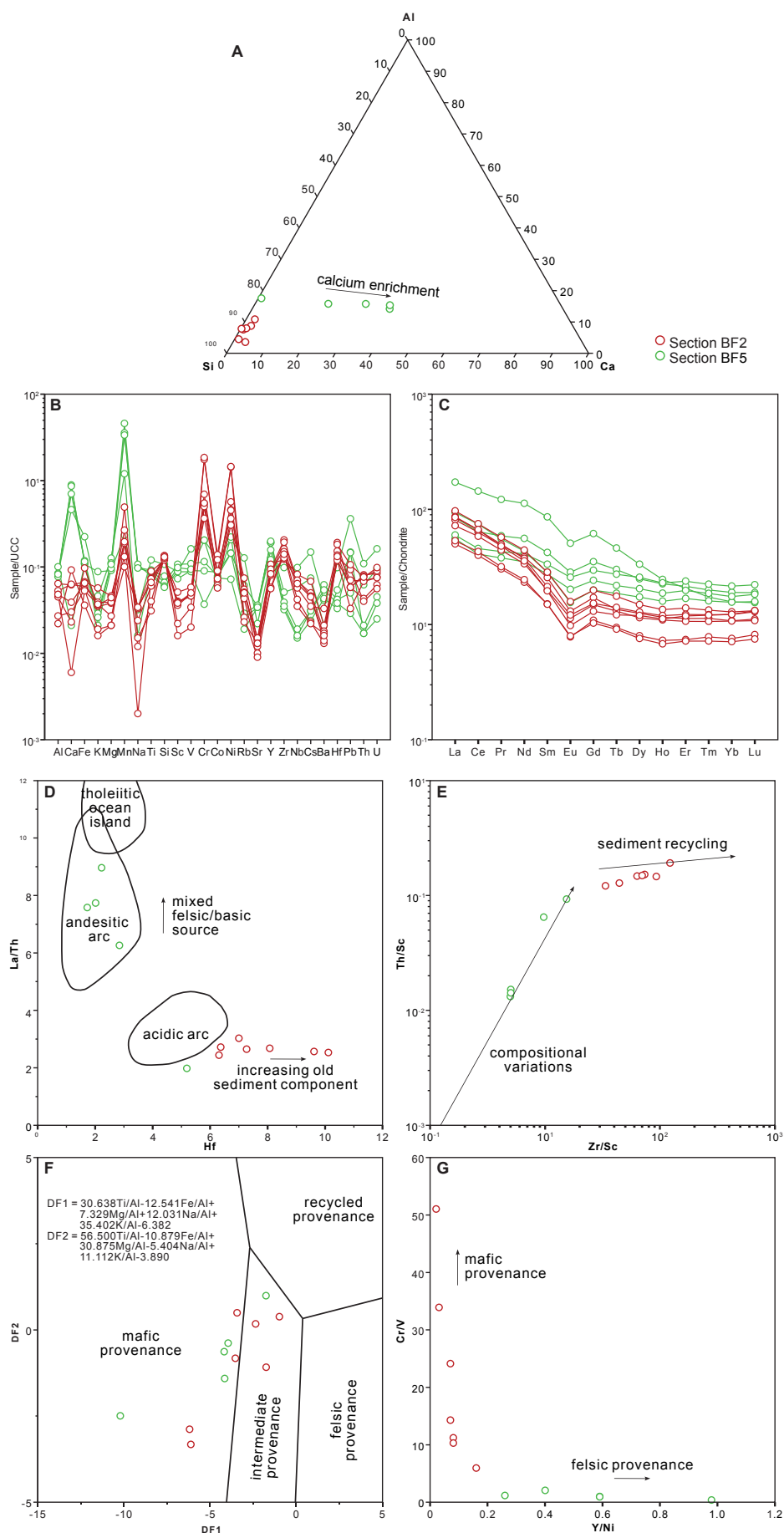
1467 Geochemical discrimination based on Pearce (2008).



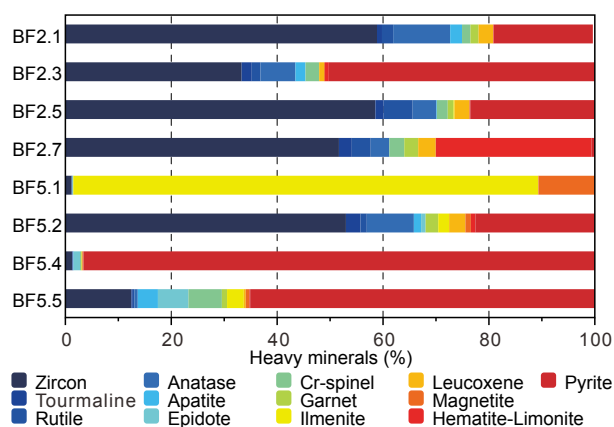
1468

1469 **Figure 5:** Correlations of radiolarian biostratigraphy in sections BC2, BC3, and BC5. Section

1470 length in meters. Time scale based on Gradstein et al. (2020).

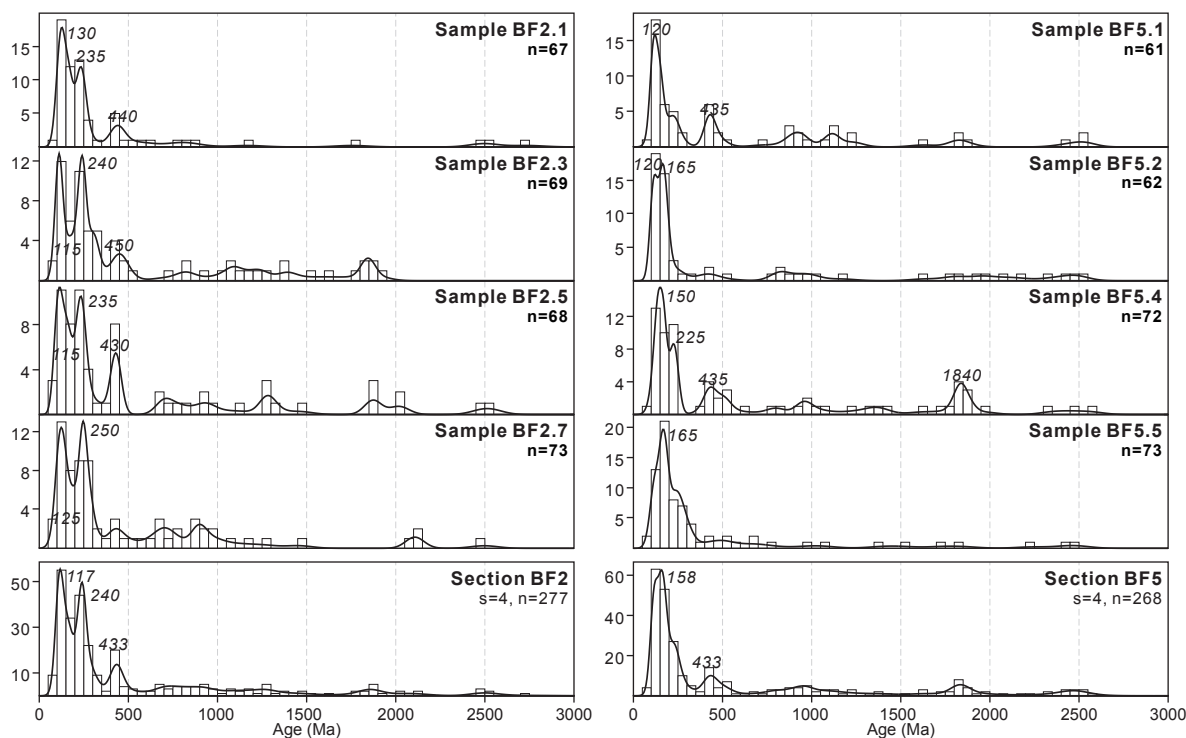


1472 **Figure 6:** Geochemistry of sandstone samples. A) Ternary diagram showing the relative
 1473 concentrations of Ca, Al, and Si of Baliojong sandstone samples. The sum of three components is
 1474 normalized to 100 (wt.%); B-C) Major and trace element and REE spider diagrams, normalized
 1475 to Upper Continental Crust (UCC; Rudnick and Gao, 2003) and Chondrite (Sun and McDonough,
 1476 1989), respectively. D-G) Element-based provenance discrimination diagrams of Baliojong
 1477 sandstone samples. (D) Hf versus La/Th plot (Floyd and Leveridge, 1987). (E) Zr/Sc versus
 1478 Th/Sc plot (McLennan et al., 1993). (F) Discriminant function diagram of major elements (Roser
 1479 and Korsch, 1988). (G) Y/Ni versus Cr/V plot (McLennan et al., 1993).
 1480



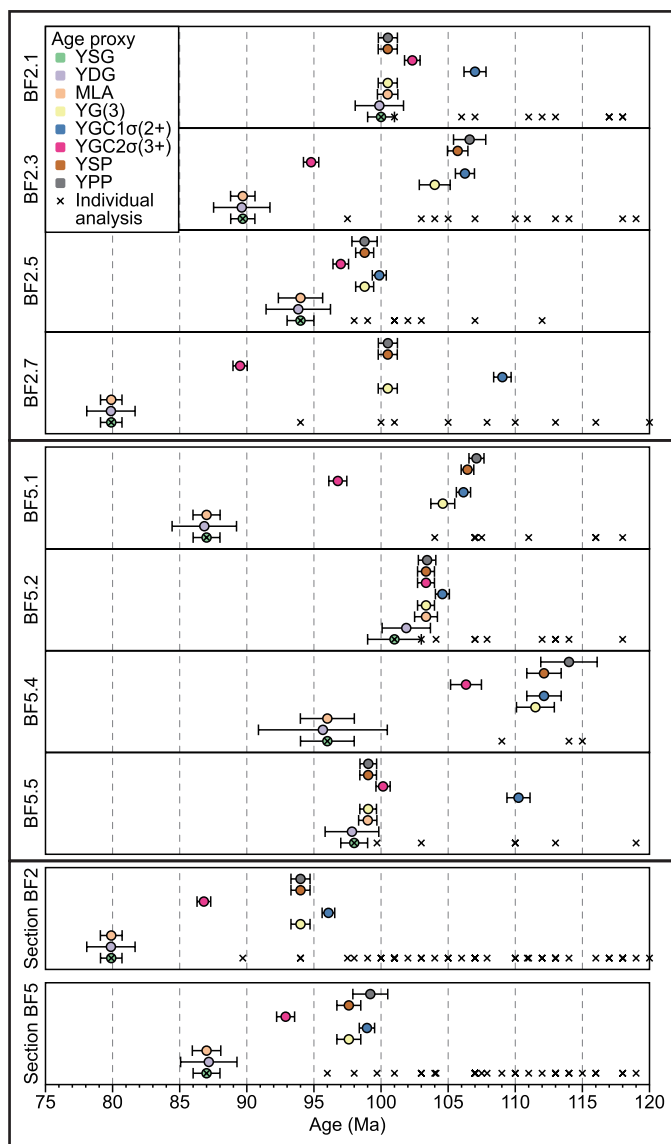
1481

1482 **Figure 7:** Relative abundance of heavy minerals of Baliojong sandstone samples.



1483

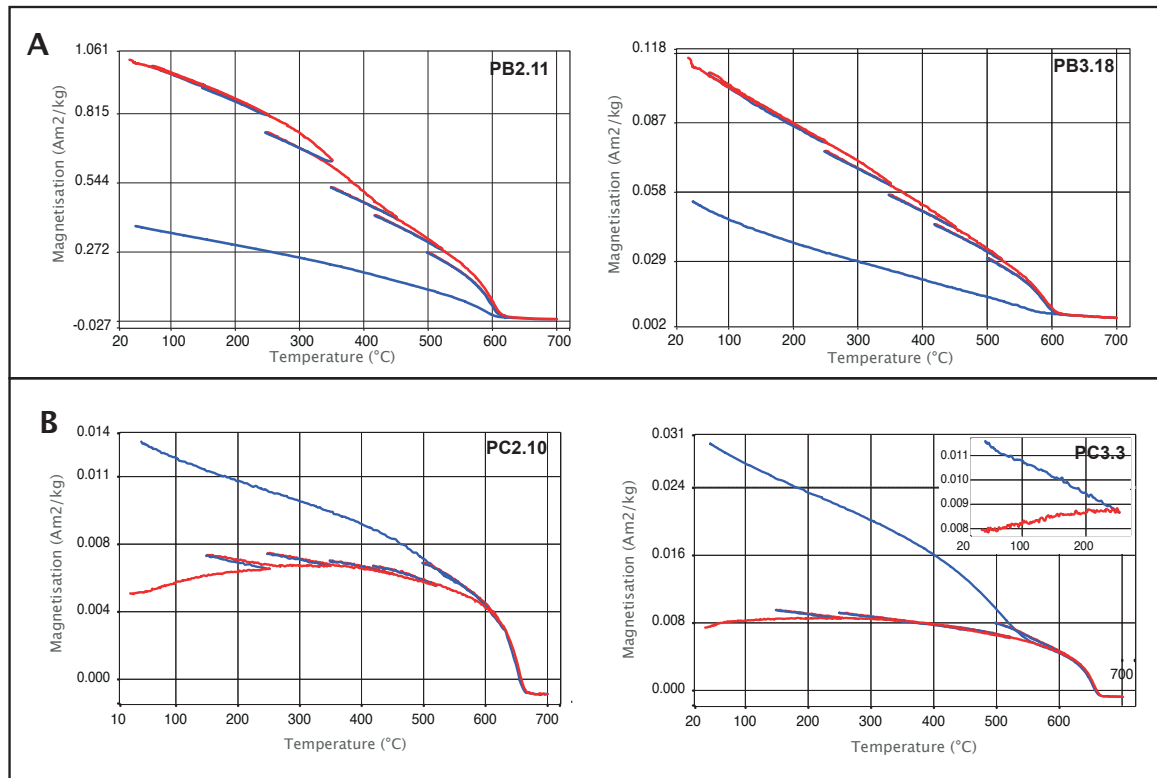
1484 **Figure 8:** Histograms and kernel density estimation (KDE) spectra for detrital zircon U-Pb ages
 1485 of Baliojong sandstone samples from sections BF2 and BF5. s—number of samples; n—number
 1486 of concordant analyses.



1487 **Figure 9:** Maximum depositional ages of Baliojong sandstone samples and grouped samples of
 1488 sections BF2 and BF5, represented by a range of age proxies of detrital zircon U-Pb
 1489 geochronology. Age proxies are calculated and visualized at 1σ and individual analyses of ≤ 120
 1490 Ma are also shown for comparison. YSG—the youngest single grain age; YDG—the age
 1491 calculated by the 'Youngest Detrital Zircon' routine of Isoplot (Ludwig, 2003); MLA—the age
 1492 calculated by 'Maximum Likelihood Age' algorithm of IsoplotR (Vermeesch, 2020); YG(3)—the
 1493 weighted mean age of three youngest grains (Zhang et al., 2015); YGC $1\sigma(2+)$ —the weighted
 1494 mean age of youngest cluster with two or more grains overlapping in age at 1σ (Dickinson and
 1495 Gehrels, 2009); YGC $2\sigma(3+)$ —the weighted mean age of youngest cluster with three or more
 1496 grains overlapping in age at 2σ (Dickinson and Gehrels, 2009); YSP—the weighted mean age of
 1497

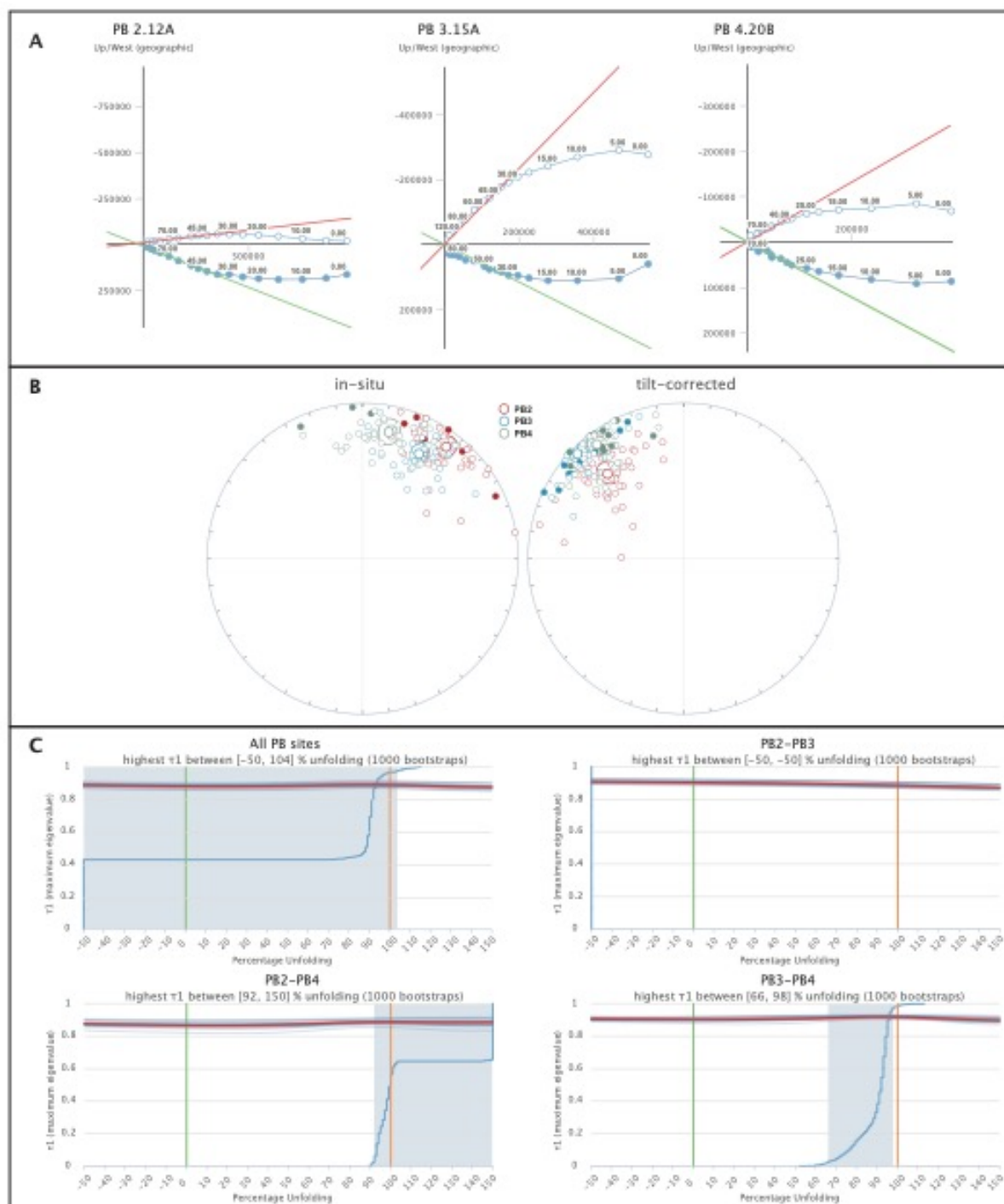
1498 youngest cluster with a mean square weighted deviation (MSWD) of ~ 1 (Coutts et al., 2019);

1499 YPP—the youngest graphic peak age of kernel density estimation (KDE) spectrum.

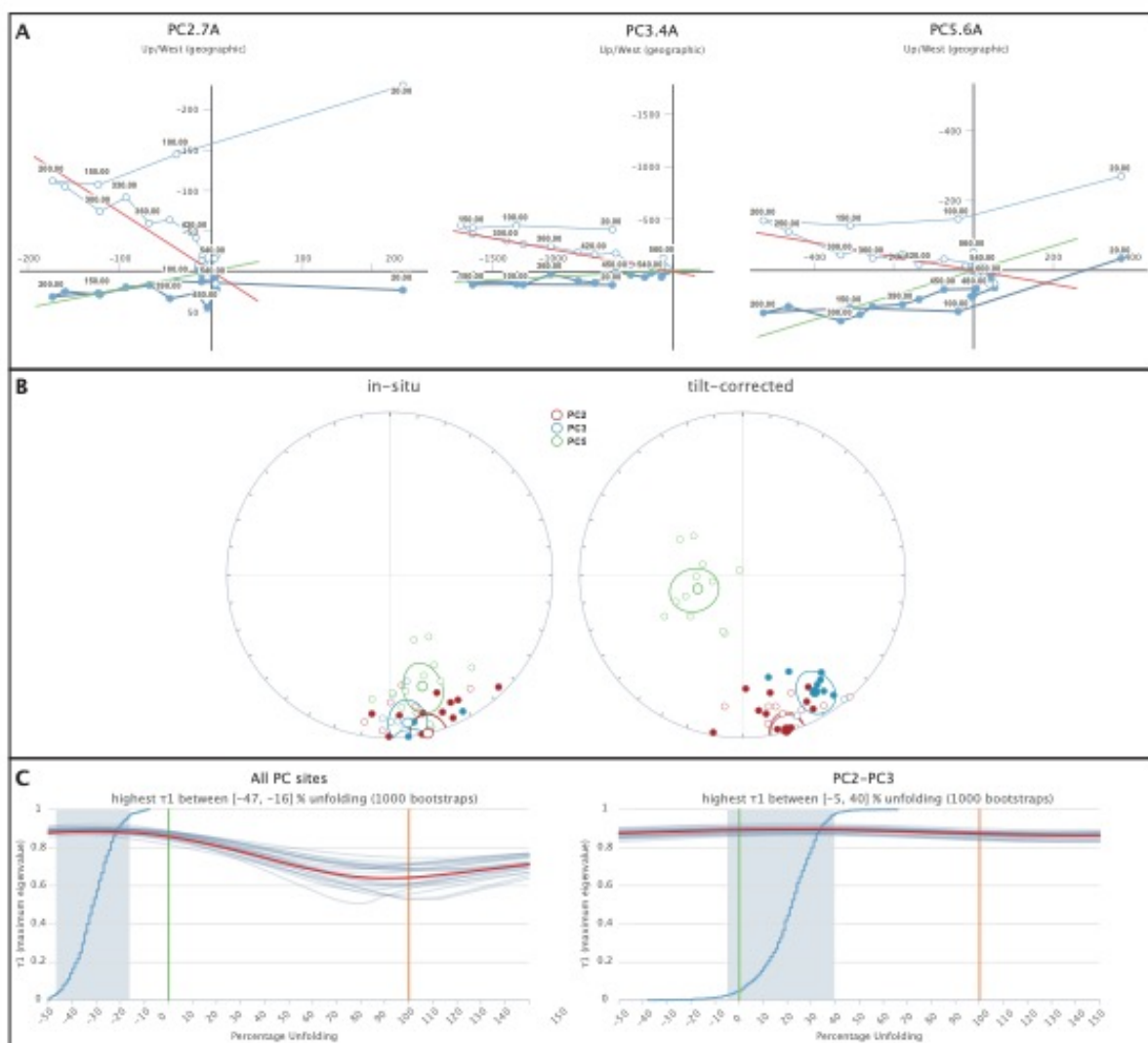


1500

1501 **Figure 10:** Thermomagnetic curves measured on a modified horizontal translation Curie
1502 balance (Mullender et al., 1993). Heating segments in red, cooling in blue. Inset in PC3.3 shows
1503 the first heating cycle to 250°C as part of the stirring experiment (see main text).



1504
 1505 **Figure 11:** Paleomagnetic results from PB sections; A) Orthogonal vector diagrams of selected
 1506 samples in geographic coordinates. Closed (open) symbols for declination (inclination); B)
 1507 Characteristic remanent magnetization (ChRM) directions, including means, per section in
 1508 geographic (in-situ) and tectonic (tilt-corrected) coordinates; C) Results of bootstrapped fold
 1509 tests for different combinations of sections.



1510

1511

1512

1513

1514

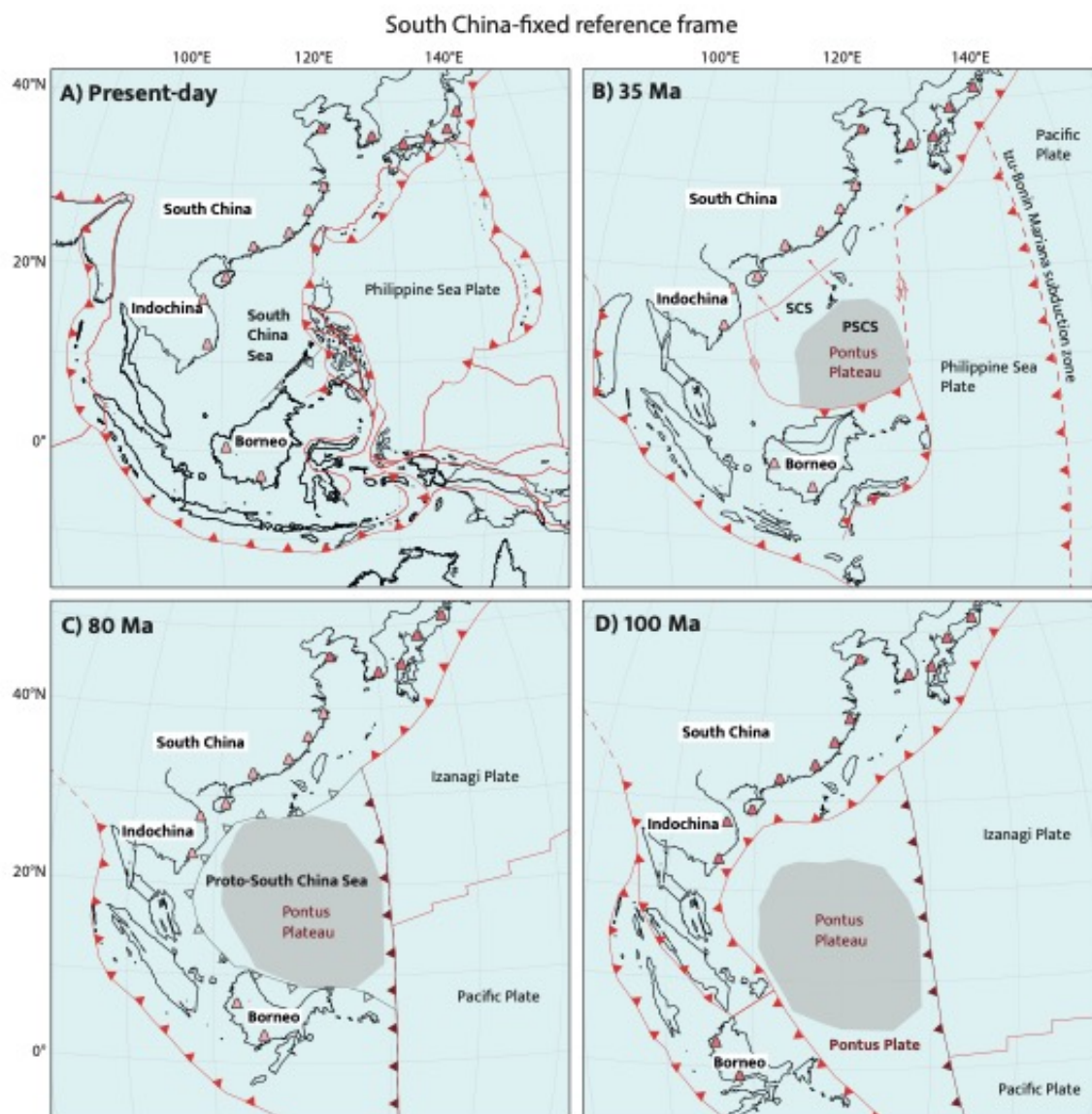
1515

Figure 12: Paleomagnetic results from PC sections; A) Orthogonal vector diagrams of selected samples in geographic coordinates. Closed (open) symbols for declination (inclination); B) Characteristic remanent magnetization (ChRM) directions, including means, per section in geographic (in-situ) and tectonic (tilt-corrected) coordinates; C) Results of bootstrapped fold tests for all PC sites and for PC2 and PC3.



1516

1517 **Figure 13:** Simplified tectonic reconstruction showing the reconstructed positions of the
1518 Baliojong River basalts as part of the Izanagi Plate and as part of a separate plate at 135 Ma.
1519 Reconstruction is made using the reconstructions of Advokaat and Van Hinsbergen (2023) and
1520 Boschman et al. (2021), in the paleomagnetic reference frame of Vaes et al. (2023). The
1521 uncertainty in the reference frame is $\sim 1^\circ$, which is smaller than the star.



1522
 1523 **Figure 14:** Simplified Late Mesozoic - Cenozoic tectonic evolution of the NW Panthalassa region,
 1524 including the Pontus Plate and the Pontus-Izanagi subduction zone, in a South China-fixed
 1525 reference frame. Reconstruction of SE Asia based on Advokaat and Van Hinsbergen (2023).
 1526 Dark pink cones indicate active arc magmatism, light pink cones indicate extinct arc
 1527 magmatism. Active plate boundaries in red, former plate boundaries in gray. New tectonic
 1528 features based on this study in dark red.